Wiley Analytical Science Virtual Conference

November 9-17

For the 3rd time, The Wiley Analytical Science Conference is back!

It's all happening November 9 - 17

The Wiley Analytical Science Virtual Conference will bring together thousands of researchers and practitioners to share current developments in science and industry. Join for exciting presentations from experts in the fields of analytical and bioanalytical chemistry, pharmaceutical research, materials science, lab automation, and related disciplines.

Register to learn about recent developments & applications in:

- Microscopy
- Spectroscopy
- Mass Spectrometry
- Separation Science
- Much more!

Register here

WILEY

Transition Metal Oxide Anodes for Electrochemical Energy Storage in Lithium- and Sodium-Ion Batteries

Shan Fang, Dominic Bresser, and Stefano Passerini*

Lithium-ion batteries (LIBs) with outstanding energy and power density have been extensively investigated in recent years, rendering them the most suitable energy storage technology for application in emerging markets such as electric vehicles and stationary storage. More recently, sodium, one of the most abundant elements on earth, exhibiting similar physicochemical properties as lithium, has been gaining increasing attention for the development of sodium-ion batteries (SIBs) in order to address the concern about Li availability and cost—especially with regard to stationary applications for which size and volume of the battery are of less importance. Compared with traditional intercalation reactions, conversion reaction-based transition metal oxides (TMOs) are prospective anode materials for rechargeable batteries thanks to their low cost and high gravimetric specific capacities. In this review, the recent progress and remaining challenges of conversion reactions for LIBs and SIBs are discussed, covering an overview about the different synthesis methods, morphological characteristics, as well as their electrochemical performance. Potential future research directions and a perspective toward the practical application of TMOs for electrochemical energy storage are also provided.

1. Introduction

Rechargeable lithium-ion batteries (LIBs) have become the common power source for portable electronics since their first commercialization by Sony in 1991 and are, as a consequence, also considered the most promising candidate for large-scale applications like (hybrid) electric vehicles and short- to mid-term stationary energy storage.[1–4] Due to the resulting great interest in this technology, extensive efforts have been made

to achieve further improved performance. As a result, the energy density of LIBs has continuously increased at a rate of 7–8 Wh kg^{-1} year^{-1}, already passing 250 Wh kg^{-1} at cell level (for 18650-type cells). Simultaneously, the overall cost decreased substantially from initially around 1000 € kWh^{-1} to less than 200 € kWh^{-1},[5] while a further reduction to less than 150 € kWh^{-1} is anticipated within the next 5 to 10 years[6]—or, in fact, might have been realized already following some recent newspaper articles. Nonetheless, further improvement is required for realizing a fully electrified transportation sector and eventually succeeding in transitioning to renewable energy sources only. For this reason, there is a great quest for alternative inactive and active materials, including inter alia the anode—not least because graphite, the state-of-the-art for LIBs, which is intrinsically limiting the fast charging of the full-cell.[7,8] Another important concern is related to the availability of the required elements, including inter alia lithium,[9,10] which has led to a rapidly increasing interest in alternative charge carriers—in particular, sodium.[11–13] In fact, the two technologies share several similarities and, hence, room-temperature SIBs are considered a "drop-in technology," as many of the achievements obtained for LIBs can be readily implemented for SIBs. This has resulted in rapid progress for the development of SIBs within only a few years. However, there are some fundamental differences between the two systems due to the different charge carriers such as the size of the cation, the standard redox potential, or simply the different cost for the corresponding precursors—as summarized briefly in **Table 1**. These affect, respectively, the diffusion and transport properties, the maximum achievable energy density, or the price of the cell. Furthermore, the different reactivity of the two systems eventually also has an effect on the (decomposition) reactions at the interface between the electrode and the electrolyte, including the charge transfer and cation desolvation, before entering the host structure. With respect to the potential host structure for the negative electrode—or in other words the electrode active material—the material classes of choice are frequently carbons (e.g., graphite or hard carbons) or metal oxides. For the latter, there are essentially three different alkali cation storage mechanisms: (i) insertion (including intercalation in case of layered structures), (ii) alloying, and (iii) conversion. In case of (i) insertion-type materials, the Li$^+$

Dr. S. Fang, Dr. D. Bresser, Prof. S. Passerini
Helmholtz Institute Ulm (HIU)
Helmholtzstrasse 11, 89081 Ulm, Germany
Dr. S. Fang, Dr. D. Bresser, Prof. S. Passerini
Karlsruhe Institute of Technology (KIT)
P. O. Box 3640, D-76021 Karlsruhe, Germany
E-mail: stefano.passerini@kit.edu

The ORCID identification number(s) for the author(s) of this article can be found under https://doi.org/10.1002/aenm.201902485.

**ADVANCED
SCIENCE NEWS**

www.advancedsciencenews.com

**ADVANCED
ENERGY
MATERIALS**

www.advenergymat.de

Table 1. Comparison of lithium and sodium regarding selected physico-chemical properties and cost.

	Lithium	Sodium
Cation radius [Å]	0.76	1.02
Relative atomic mass	6.94	22.98
$E°$ (vs SHE) [V]	−3.04	−2.71
Cost, carbonates	$5000 ton^{-1}	$150 ton^{-1}
Theoretical capacity of metal electrodes [mAh g^{-1}]	3829	1165
Coordination preference	Octahedral and tetrahedral	Octahedral and prismatic
Desolvation energy in PC [kJ mol^{-1}]	218.0	157.3

and Na$^+$ cations can be reversibly stored in the host material without any severe (irreversible) deterioration of the initial crystal structure and very low volume variation, which commonly allows for excellent cyclability and good capacity retention; also due to the commonly rather low number of Li$^+$/Na$^+$ inserted by unit weight and volume. The most classic insertion-type metal oxide anodes are based on titanium (e.g., TiO$_2$[14] and Li$_4$Ti$_5$O$_{12}$[15–17] or Na$_2$Ti$_3$O$_7$[18–21]) as redox active center, which is reduced to Ti^{3+} upon lithiation/sodiation and reoxidized to Ti^{4+} when the alkali metal cations are subsequently deinserted again. Considering the rather high mass of these compounds in combination with the relatively limited lithium/sodium uptake, however, the use of these materials is essentially limited to high-power rather than high-energy applications[22] or applications for which cycling stability is more important than energy density.[23,24] Differently, (ii) alloying-type materials (like Si, Sn, Ge, or Zn) provide high to very high—and frequently fast—lithium and sodium storage capacities, commonly exceeding one lithium or sodium per atom of the alloying element (e.g., Li$_{15}$Si$_4$ or Li$_{4.4}$Sn). Nevertheless, the accompanying extensive volume variation limits the cycle life of such electrodes—not least as a result of the continuous exposure of fresh surfaces to the electrolyte, resulting in an ongoing electrolyte decomposition and solid electrolyte interphase (SEI) formation and, as a consequence, the drying out of the cell.[4,25,26] In an attempt to (partially) overcome this issue, the use of the corresponding metal oxides had been proposed (e.g., SiO$_x$, SnO$_2$, GeO$_2$, ZnO).[27–30] The initially formed Li$_2$O was supposed to buffer the volume variation occurring upon the subsequent alloying of the elemental metal/metalloid and provide an in situ generated ion conducting matrix. However, such matrix does not prevent another issue of alloying-type materials, i.e., the continuous aggregation of the elemental particles upon de/lithiation/sodiation, which eventually still leads to rapid capacity degradation.[28,31] This issue is avoided for transition metal oxides (TMOs), for which the elemental transition metal (TM) does not alloy with lithium/sodium. Instead, the thus created metallic nanonetwork allows for a good electron conduction within the original primary particle and, by this, allows for the reversible cycling of the initially formed Li$_2$O.[4,32,33] Advantageously, this comes with significantly less volume changes upon de/lithiation/sodiation while also allowing for capacities approaching 1000 mAh g^{-1} (e.g., Fe$_2$O$_3$) thanks to the multielectron transfer reaction per TM occurring upon the conversion of

Shan Fang received her Ph.D. degree in 2018 in Nanjing University of Aeronautics and Astronautics (China). Previously, her research focused on nanostructured alloying anode materials for high energy density lithium-ion batteries. Currently, she is a post-doc fellow at the Karlsruhe Institute of Technology, Helmholtz Institute Ulm (Germany) in the research group of Electrochemistry of Batteries with Prof. Stefano Passerini. Her research aims at improving the stability of lithium metal anode by exploring artificial solid electrolyte interphase and optimized microstructures, and through the study of the mechanisms related to their performance.

Dominic Bresser is serving as group leader at the Helmholtz Institute Ulm (HIU), affiliated with the Karlsruhe Institute of Technology (KIT), Germany, focusing especially on the development of alternative anode materials, polymer electrolytes, and aqueous cathode processing technologies for lithium batteries. Prior to this, he held a postdoctoral position and Eurotalents Fellowship at CEA in Grenoble, France, after he completed his Ph.D. at Muenster University, Germany.

Stefano Passerini is professor at the Karlsruhe Institute of Technology. His research activities are focused on electrochemical energy storage with special focus on improving the sustainability of high-energy batteries.

TMOs to TM^0 and lithium/sodium oxide.[4,34–36] These unique features in combination with the richness of materials synthesis and design for such transition metal oxides has triggered a remarkable attention in the past almost 20 years since the first report on this mechanism by Tarascon and co-workers.[32] Accordingly, there has been a series of review articles in the past years on this subject.[4,34,37–39] Cabana et al.,[34] for instance, provided a very comprehensive overview on the conversion

mechanism for lithium-ion batteries until 2010, which has been updated with a clear focus on new mechanistic insights by Bresser et al.[4] in 2016. An overview organized by following the periodic table has been presented by Nitta and Yushin,[35] for example. Similarly, very comprehensive review articles on (conversion-type) anode materials for sodium-ion batteries have been published in the past—partially more generally covering all potential negative material candidates,[40,41] partially with a particular focus on (nanostructured) conversion and alloying materials.[33] A comprehensive comparison of TMO negative electrodes with a clear focus on the conversion-type lithium and sodium storage, however, has been missing so far. Accordingly, this review article is organized as follows: First, we provide the reader with a general introduction into the reaction mechanism as such, including the major advantages and remaining challenges. Subsequently, we provide an overview on the most relevant TMOs for use as negative electrodes in lithium-ion and sodium-ion batteries with particular attention toward recent publications that have not been covered by the abovementioned review articles so far. Finally, we conclude this review with a brief summary and an opinionated perspective toward the potential application of TMO negative electrodes in commercial lithium-ion and sodium-ion battery cells.

2. Potential Advantages and Challenges of the Conversion Mechanism

In 2000, Tarascon and co-workers[32] reported a new Li$^+$ storage mechanism involving the reversible electrochemical lithiation of TMOs (TM = Co, Ni, Fe, Cu). According to the main reaction, the process is generally referred to as a "conversion reaction," formally as follows

$$TM_aX_b + (b \cdot n)AM \leftrightarrows aTM + bAM_nX \tag{1}$$

with TM being a transition metal (e.g., Fe, Co, Mn, Cu, Ni), AM an alkali metal (e.g., Li, Na), X an anion (such as H, N,

P, O, S, F), and n as the formal oxidation state of X. Since the transition metal is generally reduced to the metallic state, involving the transfer of several electrons per unit formula of the starting compound, conversion reactions commonly show much higher capacities than intercalation reactions. In case of Co_3O_4, for example, the complete reduction of Co^{2+}/Co^{3+} in a Li$^+$-containing electrolyte leads to the formation of Co^0 and Li_2O, which corresponds to an overall specific capacity of 890.4 mAh g^{-1} (based on Co_3O_4). This value is about three times higher than the capacity based on a classical intercalation reaction as in case of $LiCoO_2$ (273.8 mAh g^{-1}) for which Co^{3+} is reversibly oxidized to Co^{4+}. In practice, in fact, even less capacity is achieved, as only about 0.5 lithium can be reversibly extracted without severely deteriorating the crystalline structure of the host lattice. Adelhelm and co-workers[36] investigated the impact of the alkali metal on the conversion reaction. The standard cell potential $E°$ can be calculated using

$$E° = -\frac{\Delta_r G°}{zF} \tag{2}$$

Accordingly, they conducted a direct comparison of the cell voltages for lithium and sodium. It has been recognized that the change in cell voltage is constant for oxides, fluorides, hydrides, etc., when replacing lithium with sodium. For example, the change in cell voltage for oxides is 0.96 V, as shown in Reaction (3)

$$2Li + Na_2O \leftrightarrows Li_2O + 2Na \quad \Delta E(Li - Na): 0.96\ V \tag{3}$$
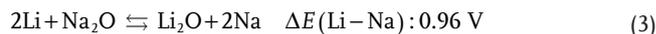
The same calculation applies generally to other conversion reactions with X = H, O, S, F, Cl, Br, and I (**Figure 1**a). When lithium is substituted by sodium in conversion reactions, the cell voltage shifts to lower values for hydrides, oxides, sulfides, and fluorides. For chlorides, the cell voltage is nearly the same, while for iodides and bromides the sodium conversion reaction shows even higher cell voltages compared to the corresponding reaction with lithium. This is remarkable, as sodium-based
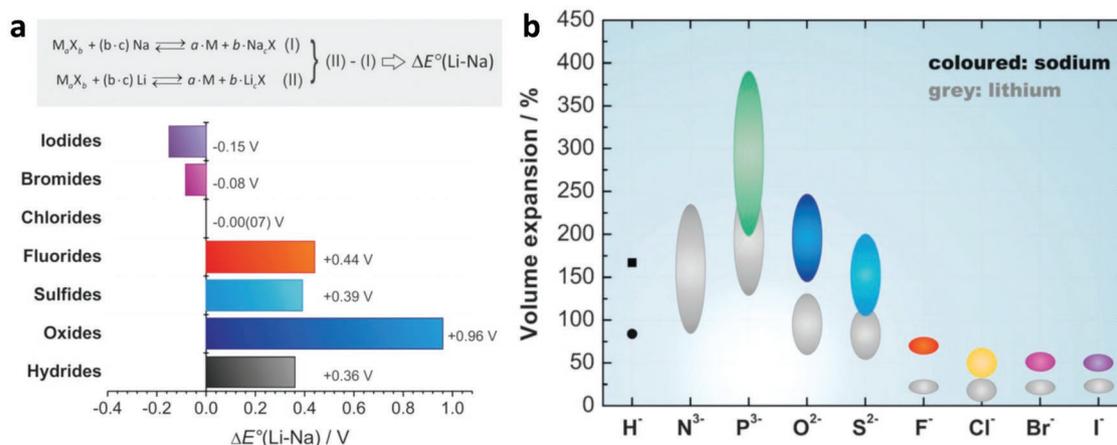
Figure 1. a) Effect of the replacement of Li by Na in conversion reactions on the corresponding redox potential for various compounds: For fluorides, sulfides, oxides, and hydrides, the reaction with lithium shows higher cell voltages in a theoretical LIB configuration. For chlorides, the difference is essentially zero and for the even heavier bromides and iodides, a hypothetical SIB is anticipated to deliver a higher cell voltage. b) Calculated volume expansions for Li and Na-based conversion reactions. Reproduced with permission.[36] Copyright 2013, Royal Society of Chemistry.

ADVANCED
SCIENCE NEWS
www.advancedsciencenews.com

ADVANCED
ENERGY
MATERIALS
www.advenergymat.de

cells are intuitively considered to provide a lower cell voltage compared to their lithium analogues. This behavior can be reasonably explained in consideration of the associated Born–Haber cycles.[36] The lithium compounds have larger lattice energies than the corresponding sodium versions, resulting in greater negative Gibbs reaction energies, which then translates to higher cell voltages. Nevertheless, this difference might be compensated or even overcompensated in case of the chlorides and bromides/iodides, respectively, as a result of the lower ionization and cohesive energy for the sodium analogues.

With respect to their employment in commercial battery cells, however, several fundamental obstacles still remain before these materials can become a viable alternative, despite the great promise of this concept in general. Among these challenges, one of the most relevant is the low initial coulombic efficiency (CE), which is commonly below 75% and associated inter alia with the strong structural reorganization. The initial lithiation results in the formation of the corresponding metallic nanoparticles being distributed in the simultaneously formed amorphous AM_nX matrix.[32] During the first lithiation also the solid electrolyte interphase (SEI) layer occurs on the surface of the electrode, which is composed of decomposition products of the utilized electrolyte. Depending on the nature and structure of the electrode active material as well as the current applied, the lithiation reaction may include one or more intermediate phases. Another main obstacle, and even more important limitation, is the poor energy efficiency of the AM storage process due to large polarization effects and/or different reaction pathways.[4] Overpotentials appear to be intrinsic to conversion reactions and their magnitude increases with the bond polarity. For fluorides, for example, the combined overpotentials can exceed 1 V,[5] which results in a rather low round-trip energy efficiency. In addition, the conversion reaction is accompanied by considerable volume changes. The effect on halides is minimal (generally less than 50%), while for sulfides or oxides, the volume expansion may exceed 100%, potentially causing significant mechanical deterioration of the electrode (Figure 1b). These volume changes are even more severe for sodium, i.e., approximately twice as high. Thus, it is anticipated that the development of suitable conversion materials for SIBs will be even more demanding than for LIBs. At this point, we may note again that the conversion mechanism, as generalized in Reaction (1), frequently involves an initial Li^+ insertion,[42] leading characteristic nanostructures. Accordingly, diffusion distances stay short, enhancing the reversibility of the conversion reaction.[43] In contrast, the formation of relatively large TM^0 particles may negatively affect the rechargeability. Replacing Li^+ by Na^+ will certainly have an important influence on this initial insertion mechanism and the subsequent reaction steps—even though this requires further investigation.

In fact, the hope that replacing Li by Na might help to overcome the challenges for Li-involving conversion reactions has not become true so far and only a few studies have specifically focused on such a direct comparison between Li and Na. In general, the capacities obtained for the Na analogues are lower than for the corresponding LIB configuration. For Fe_2O_3 nanoparticles, for instance, a high capacity of 1000 mAh g^{-1} was reported in the Li-configuration, which is close to the theoretical specific capacity of 1006 mAh g^{-1}, but only around 350 mAh g^{-1} were obtained for the Na-configuration. Nonetheless, this value

is still much higher than common intercalation-related capacities—especially in case of sodium.[44] Remarkably, a comparison of the reactivity with Li and Na when studying the conversion reaction for the rather little explored carbodiimide anion exhibits the reversed behavior, i.e., the capacities observed for Na exceed those for Li,[45] though the definite reason remains to be elucidated. Thus, despite the remaining challenges, conversion-type reactions are still considered a promising field of research, particularly with regard to the potential use of cost-efficient and abundant materials like iron oxide or sulfides.

3. Transition Metal Oxides as Anode Materials

TMOs are, by far, the class of conversion materials that has attracted most attention—presumably as a result of their ease of handling and their high capacities. Also, with respect to sodium storage, TMOs have received considerable attention recently, including Fe_2O_3, Co_3O_4, MnO, CuO, and NiO. Nevertheless, the reversible capacities of oxides as sodium-ion active materials are much lower than their theoretical capacities and, as mentioned earlier, when investigated as reversible Li^+ hosts. The reaction potential, however, is commonly lower for the reversible sodium storage,[46] rendering them more suitable as anode materials compared to their lithium analogues, which is consistent with theoretical calculations based on thermodynamic data. According to the reported literature, the reversible capacities of oxides are obtained at voltages lower than 2 V. Besides such "intrinsic" values, in both cases, modifying the electrode structure or the incorporation of additional conductive materials are effective strategies to improve the reaction kinetics.

In the following, the most promising oxide materials as conversion anodes for LIBs and SIBs are reviewed and, as far as possible, we will provide a direct comparison of their performance. Nonetheless, due to the lack of information available in literature, such comparative analysis remains rather difficult—also as some studies are focusing less on "basic electrochemical information" and more on factors essential for the final performance, such as the areal active material loading and capacity (in mg cm^{-2} or mAh cm^{-2}) or the weight fraction of the nonactive components in nanostructured composites.

3.1. Iron Oxide (Fe_3O_4, Fe_2O_3)

Iron oxides, such as α-Fe_2O_3 and Fe_3O_4, are considered to be attractive candidates for the next generation of anode materials due to their abundance, nontoxicity, and low cost. Fe_2O_3, for instance, following the general reaction mechanism Fe_2O_3 + $6Li^+$ + $6e^-$ $\leftrightarrows$ $2Fe$ + $3Li_2O$ exhibits a high theoretical specific capacity of 1006 mAh g^{-1}, as reported firstly by Tarascon and co-workers.[32] They reported that each formula unit allows for the uptake of 0.5 mol of Li being reversibly inserted into nano-α-Fe_2O_3 (20 nm) in the voltage range between 1.5 and 4.0 V. When extending the voltage range to 0.005–3.0 V, 8.5 mol of Li mole^{-1} of Fe_2O_3 react, resulting in the degradation of the crystal structure and the formation of metallic iron nanoparticles and Li_2O based on the common conversion reaction. In addition, a

ADVANCED
SCIENCE NEWS
www.advancedsciencenews.com

**ADVANCED
ENERGY
MATERIALS**
www.advenergymat.de

polymeric layer on the particles was also observed, which was assigned to the electrolyte (solvents and salt) decomposition. Nanostructured metal oxides have been used to enhance the rate performance and reversible capacity, taking advantage of the shortened Li^+ transport pathways and the decreased volume changes due to the electrochemical reaction.[47] In a subsequent study, Chen et al.[48] reported the synthesis of α-Fe_2O_3 nanotubes using alumina membranes as the template. The as-prepared nanotubes with uniform size and shape and high specific surface area displayed excellent electrochemical activity, including a very high discharge capacity (1415 mAh g^{-1} at 100 mA g^{-1}). Chowdari and co-workers[49] synthesized α-Fe_2O_3 nanoflakes on copper foil by a hydrothermal method. The electrochemical tests revealed that such Fe_2O_3 nanoflakes show a reversible capacity of 680 ± 20 mAh g^{-1}, equivalent to 4.05 ± 0.05 moles of Li mole^{-1} of Fe_2O_3 with negligible capacity decay up to 80 cycles for a voltage range of 0.005–3.0 V and at a specific current of 65 mA g^{-1}. The average lithiation and delithiation potential, though, were 1.2 and 2.1 V, respectively. Cho's group[50] employed an iron-based metal–organic framework (MOF) as template and prepared spindle-like porous α-Fe_2O_3. This material showed greatly improved electrochemical performance. After 50 cycles at 0.2C, a capacity of 911 mAh g^{-1} was maintained and, even when increasing the current to 10 C, a capacity of 424 mAh g^{-1} was delivered by this electrode material. Balducci and co-workers[51] investigated the electrochemical charge/discharge mechanism

of hematite and found that at the end of the delithiation process, lithium iron oxide (α-$LiFeO_2$) was formed, thus providing an additional source of irreversible capacity loss (**Figure 2**a–c). Backert et al.[52] reported a graphene-wrapped Ni@Fe_2O_3 composite, employing sulfonated reduced graphene oxide. The developed complex material showed highly improved electrochemical performance, offering a capacity of 1051 mAh g^{-1} after 40 cycles at 50 mA g^{-1}. Lou and co-workers[53] synthesized Fe_2O_3 hollow structures, including hollow microboxes and spheres. When evaluated as anode material for LIBs, these well-defined hollow structures exhibited remarkable cycling performance with high specific capacity. Such hierarchical hollow architectures allow for shortening the diffusion pathways for the Li cations and may, moreover, accommodate the volume variation occurring upon cycling. Various carbon additives have also been mixed with the metal oxide particles to enhance their electronic conductivity.[54] Wang et al.[55] reported an advanced carbon-coated CNT@Fe_2O_3 hierarchical nanostructure. This material was constructed through the bottom-up assembly of β-FeOOH nanospindles on the CNT framework. After the thermal treatment, carbon-coated hollow α-Fe_2O_3 nanohorns were obtained. Thanks to the greatly improved kinetics and electrode stability, this hybrid structure exhibited a stable capacity retention of 800 mAh g^{-1} after 100 cycles at a specific current of 500 mA g^{-1} and excellent rate performance. Following these promising studies on Fe_2O_3 as a potential anode candidate, a few studies
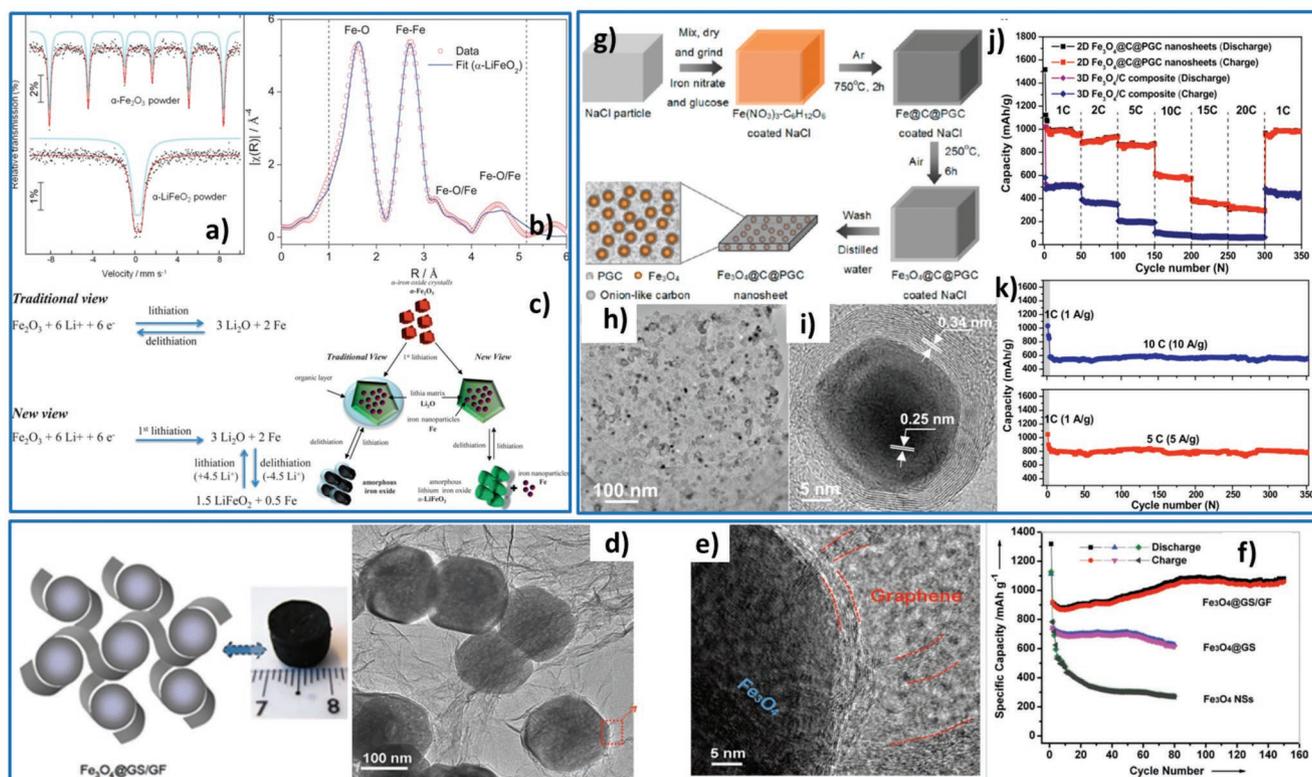
Figure 2. a) Experimental and simulated ^{57}Fe Mossbauer spectra of pristine α-Fe_2O_3 and the cycled (delithiated) electrode at 298 K in comparison with powdered α-$LiFeO_2$, indicating the formation of α-$LiFeO_2$ upon cycling, as also confirmed by b) EXAFS analysis and fitting. c) Summary of the de/lithiation reaction mechanism for carbon-coated Fe_2O_3. Reproduced with permission.[51] Copyright 2013, The Royal Society of Chemistry. d) Schematic illustration, photograph, TEM, and e) HRTEM images of Fe_3O_4@GS/GF and f) its cycling performance. Reproduced with permission.[60] Copyright 2013, Wiley. g) The fabrication procedure of 2D Fe_3O_4@C@PGC. h,i) TEM and HRTEM images of the resulting composite. j,k) Rate capability and constant current cycling performance of Fe_3O_4@C@PGC electrodes. Reproduced with permission.[64] Copyright 2013, American Chemical Society.

**ADVANCED
SCIENCE NEWS**

www.advancedsciencenews.com

**ADVANCED
ENERGY
MATERIALS**

www.advenergymat.de

analyzed the performance in lithium-ion full-cells. For example, Aravindan et al.[56] fabricated LIBs using 1D Fe_2O_3 as the anode active material and $Li_{1.33}Ni_{0.5}Mn_{1.5}O_4$ for the cathode. Before assembling the full-cells, the authors overlithiated the cathode with a certain amount of Li (0.33 mol) to compensate the irreversible capacity loss occurring at the anode. Such full-cells delivered a specific energy of 193 Wh kg^{-1} and an average cell voltage of 3.27 V and showed a capacity retention of 88% after 60 cycles. Verrelli et al.[57] combined a Fe_2O_3-MCMB composite with $Li_{1.35}Ni_{0.48}Fe_{0.1}Mn_{1.72}O_4$ as cathode, resulting in a Li-ion full-cell with an operating voltage of ≈3 V, high CE, and a stable capacity of about 100 mAh g^{-1}, which translates into a theoretical gravimetric energy density of 300 Wh kg^{-1}.

Besides Fe_2O_3, also Fe_3O_4 has been intensively studied as anode material in lab-scale LIBs, since it has a high theoretical capacity as well (925 mAh g^{-1}). Just like Fe_2O_3, the realization of nanostructured particle architectures has been considered as an efficient way to enhance its electrochemical properties. For instance, Liu et al.[58] developed uniform pomegranate-like nanoclusters composed of ultrafine Fe_3O_4@nitrogen-doped carbon (Fe_3O_4@N-C) subunits with a diameter of around 4 nm prepared by a facile one-pot method. Compared with the reference core–shell nanoparticles, this unique structure provided even shorter Li^+ and electron diffusion pathways, further enhanced structural stability during cycling, and high electronic conductivity. As a result, this pomegranate-like Fe_3O_4@N-C possessed good rate performance and capacity retention upon long-term charge–discharge tests at specific currents of 1 A g^{-1} (1063.0 mAh g^{-1} and 98.4% capacity retention after 1000 cycles), 10 A g^{-1} (606.0 mAh g^{-1} with 92.0% capacity retention after 1000 cycles), and 20 A g^{-1} (417.1 mAh g^{-1} with 91.7% capacity retention after 1000 cycles). 3D graphene foams have also been widely used in energy storage materials, since the highly porous structure can alleviate the pulverization of the metal oxides induced by volumetric changes and contribute to the electronic conductivity.[59] Feng and co-workers[60] described a novel approach to synthesize 3D graphene foams (GF) cross-linked with Fe_3O_4 nanospheres (Fe_3O_4 NSs) and encapsulated in graphene sheets (Fe_3O_4@GS; Figure 2d,e). In such hierarchical Fe_3O_4@graphene-sheets/graphene-foam (Fe_3O_4@GS/GF) hybrids, the double protection helps to alleviate the volume changes occurring during the electrochemical processes. The graphene shells suppress the aggregation of Fe_3O_4 NSs and buffer the volume changes, while the interconnected 3D graphene network reinforces the core–shell structure of Fe_3O_4@GS and improves the overall electronic conductivity of the electrode. Therefore, such a composite achieves a high reversible capacity of 1059 mAh g^{-1} over 150 cycles with excellent rate capability (Figure 2f). Besides these complex hierarchical structures, simple carbon coating is a widely used approach to modify the surface of active materials, as it can significantly improve the electronic conductivity of the electrode materials and reduce, if not avoid, side reactions at the particles surface.[61,62] Wan and co-workers[63] synthesized carbon-coated Fe_3O_4 nanospindles via the partial reduction of carbon-coated hematite nanospindles. The resulting Fe_3O_4-C nanospindles displayed a stable capacity of ≈600 mAh g^{-1} at C/2, which was fully retained after 80 cycles. He et al.[64] fabricated carbon-encapsulated Fe_3O_4 nanoparticles embedded in 2D highly conducting

porous graphitic carbon nanosheets (NSs) (Fe_3O_4@C@PGC nanosheets) using NaCl as template (Figure 2g–i). In such an architecture, the thin carbon layers prevent the direct contact between the Fe_3O_4 active material and the electrolyte, thus, preserving the structural and interfacial characteristics of the Fe_3O_4 nanoparticles. At the same time, the electronically conductive and flexible PGC nanosheets can alleviate the volume changes of the Fe_3O_4@C nanoparticles and prevent their deleterious aggregation through maintaining the electrical and overall structural integrity of the composite electrode upon cycling. Electrodes based this composite exhibit very high cycling stability and rate capability (Figure 2j,k). A full-cell of porous carbon-Fe_3O_4/Li[$Ni_{0.59}Co_{0.16}Mn_{0.25}$]$O_2$ was developed by Ming et al.[65] The cell showed a high specific capacity of ≈150 mAh g^{-1} and high energy density of 483 Wh kg^{-1} (working voltage ≈ 3.2 V). An anode consisting of Fe_3O_4 nanoparticles coated with a layer of F-doped carbon (Fe_3O_4@CF$_x$) and coupled with a $LiNi_{0.5}Mn_{1.5}O_4$ cathode has also been investigated.[66] Such full-cell provides a gravimetric energy density of 371 Wh kg^{-1} accompanied by a capacity retention of 66.8% after 300 cycles at 100 mA g^{-1}.

Following these promising results, iron oxides have also been studied as anode materials in SIBs. Chen and co-workers,[67] for instance, reported the synthesis of a porous 3D γ-Fe_2O_3@C nanocomposite, using an aerosol-assisted method, and demonstrated its promising performance for SIBs. The resulting electrodes showed a reversible capacity of 740 mAh g^{-1} after 200 cycles at 200 mA g^{-1}. Even after 1400 cycles at high currents (i.e., 2 A g^{-1}) the electrodes maintained a reversible capacity of 358 mAh g^{-1} (**Figure 3**a–d). Jiang et al.[68] investigated a series of thin-film TMOs, such as Fe_2O_3, NiO, Co_3O_4, and Mn_3O_4, all showing high electrochemical activity as anodes in SIBs. Especially Fe_2O_3 delivered a high capacity of 386 mAh g^{-1} at 100 mA g^{-1} after 200 cycles. A reversible capacity of 233 mAh g^{-1} was achieved even at a very high specific current of 5 A g^{-1}. Park and Myung[69] examined carbon-coated Fe_3O_4 dispersed on CNTs for both lithium and sodium storage. Used in SIBs, this material displayed a good rate capability at high current (196 mAh g^{-1} at 2.4 A g^{-1}). Zhou et al.[70] developed Fe_3O_4 and Co_3O_4 nanocrystals embedded in carbon spheres prepared by a biochemistry method using recombinant elastin-like polypeptides (containing hexahistidine) and further carbonization. The active material particles with a diameter of ≈5 nm were homogeneously distributed in the carbon matrix. This unique structure exhibited encouraging sodium storage capacity, i.e., 309 mAh g^{-1} after 100 cycles at 0.5 A g^{-1}. Liu et al.[71] reported the synthesis of a 3D-0D graphene-Fe_3O_4 quantum dot composite, constituted by Fe_3O_4 quantum dots (≈4.9 nm) anchored on the surface of 3D structured graphene nanosheets. The composite exhibited ultrahigh sodium storage capacity and outstanding cycling performance (Figure 3e–j). Qin et al.[72] successfully prepared chain-like Fe_3O_4/C/red-P by employing a magnetic field. This treatment helped to tune the orientation of the chain-like arrays on the current collector to optimize the electrochemical performance, providing superior rate performance (692 mAh g^{-1} at 2 A g^{-1}) and good cycle-life performance (Figure 3k). Qi et al.[73] reported the synthesis of carbon-coated Fe_3O_4 nanoparticles anchored on rGO (Fe_3O_4@C/rGO). This
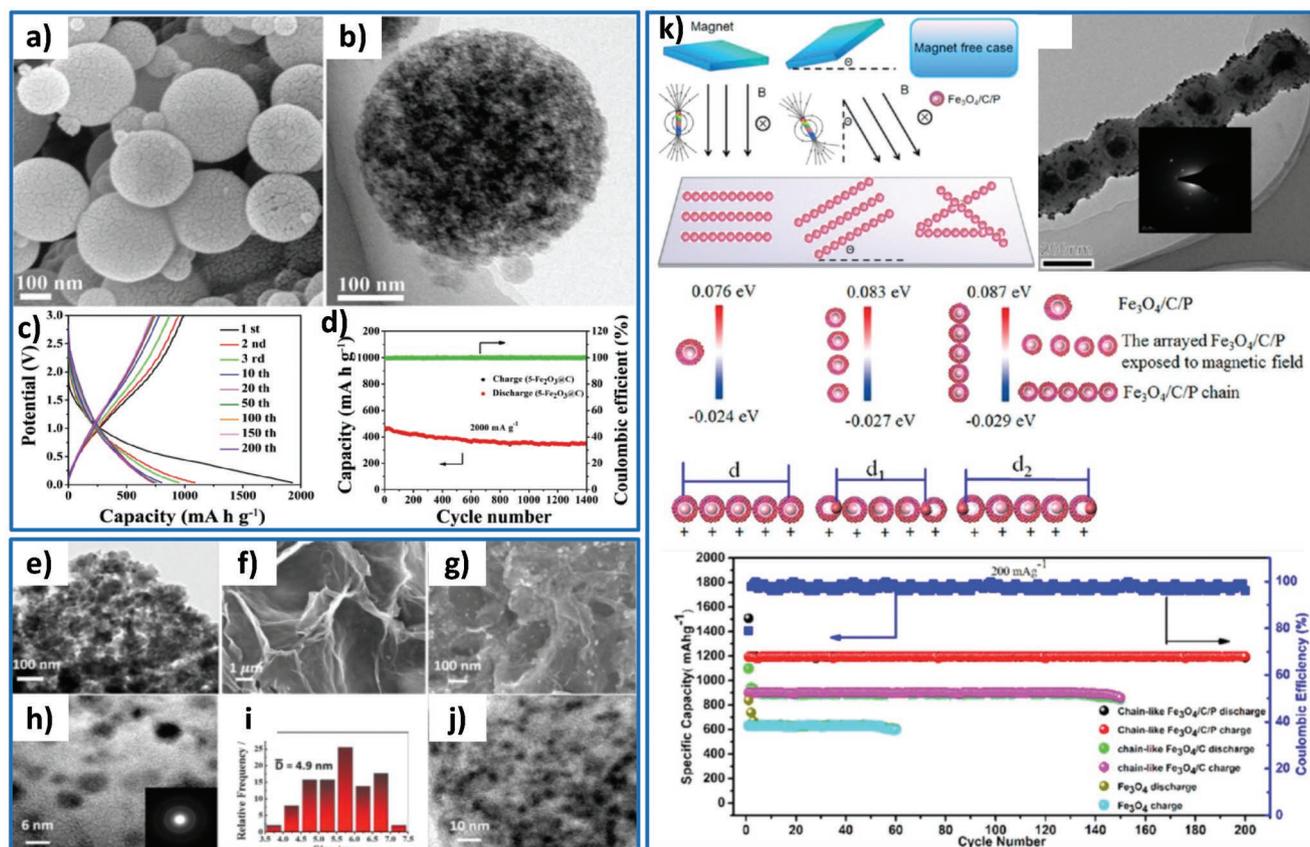
Figure 3. a,b) SEM and TEM images of $Fe_2O_3@C$ and its electrochemical performance as a sodium-ion anode: c) The dis/charge profiles of $Fe_2O_3@C$ between 0.04 and 3.0 V and d) the long-term constant current cycling performance at a voltage range of 0.04–3.0 V. Reproduced with permission.[67] Copyright 2015, Wiley. e–j) SEM and TEM images of graphene-Fe_3O_4 hybrids and i) the particle size distribution of the embedded Fe_3O_4 QDs. Reproduced with permission.[71] Copyright 2016, American Chemical Society. k) Chain-like Fe_3O_4/C/red-P assembled in the presence of a magnetic field and its long-term cycling performance. Reproduced with permission.[72] Copyright 2018, American Chemical Society.

composite delivered a capacity of 356 mAh g^{-1} as SIB anode material after 300 cycles at 0.1 A g^{-1}. Slightly superior performance was obtained for Fe_2O_3 nanoparticles encapsulated in an N-doped carbon matrix, which was synthesized using an iron-containing MOF as precursor and provided a specific capacity of 474 mAh g^{-1} at 0.1 A g^{-1} after 100 cycles.[74] Chen et al.[75] designed 1D nanocomposites with γ-Fe_2O_3 comprised in porous carbon fibers (γ-Fe_2O_3/PCF) by electrospinning. They compared the performance as Li^+ and Na^+ host and found an inferior performance in case of sodium; the capacity retention was only ≈78% after 50 cycles at 0.1 C. Better results for a similar particle morphology were obtained by Ni et al.,[76] who synthesized Fe_2O_3 nanotubes which were subsequently treated by surface sulfurization, i.e., the formation of FeS_2 (S-Fe_2O_3). The realization of such heterostructure led to a built-in electric field, which enhances the charge transfer and reduces the activation energy. When tested as anode materials for SIBs, the composite showed an excellent electrochemical performance of 91% capacity retention after 200 cycles at 5 A g^{-1}. The final evaluation in sodium-ion full-cells with a $Na_{0.67}(Mn_{0.67}Ni_{0.23}Mg_{0.1})O_2$ cathode revealed a rather promising gravimetric energy density of 142 Wh kg^{-1}. The findings of the studies reviewed herein are comparatively summarized in **Table 2**. The high abundance, potentially low cost,

environmental friendliness, facile synthesis, and richness in chemistry, including several different oxidation states available, render iron oxides a promising energy storage material. Nonetheless, the poor electronic conductivity (specifically in the de/lithiated/sodiated state) and the continuous cleavage and reformation of ionic bonds remain as major hurdles for long-term stable cycling, despite the great progress in designing nanostructured material composites including electron conducting secondary phases. In fact, as shown in Table 2, the specific capacity of iron oxides ranges between 500 and 900 mAh g^{-1} for lithium storage and ≈300 mAh g^{-1} for sodium storage. However, these high specific capacities are commonly achieved for low mass-loading electrodes and relatively limited cycle numbers. Commercial cells have to provide stable capacity for >1000 cycles ideally and capacity loadings of ≈4 mAh cm^{-2}—challenges which remain to be addressed for this material family and which require proper solutions to ensure good adhesion of the coating layer to the current collector, high mechanical stability, fast and efficient electrolyte wetting, as well as high ionic and electronic conductivities. Nevertheless, prior to addressing these "practical" issues, the main hurdles remain: (i) the investigation of the electrochemical reaction mechanism in order to overcome the large voltage hysteresis and, by this, the improvement of the

**ADVANCED
SCIENCE NEWS**

www.advancedsciencenews.com

**ADVANCED
ENERGY
MATERIALS**

www.advenergymat.de

Table 2. Overview of reported electrochemical performances for selected iron oxide-based active materials and composites.

Materials	LIBs or SIBs	Active material mass loading [mg cm^{-2}]	Composite material loading [mg cm^{-2}]	Specific capacity [mAh g^{-1}]	Specific current [mA g^{-1}]	Capacity retention (based on charge capacity)/number of cycles	Ref.
α-Fe$_2$O$_3$ nanotube	LIBs	NA	NA	510	100	36%/100	[48]
α-Fe$_2$O$_3$ nanoflakes	LIBs	0.175	0.175	680	65	83%/80	[49]
Spindle-like porous α-Fe$_2$O$_3$	LIBs	0.8	0.8	911	200	72%/50	[50]
srGO/Ni@Fe$_2$O$_3$	LIBs	2.2–2.6	NA	1051	50	76%/40	[52]
Hierarchical Fe$_2$O$_3$ microboxes	LIBs	NA	NA	945	200	80%/30	[53]
Carbon-coated α-Fe$_2$O$_3$	LIBs	1.35	1.5	820	130	99%/50	[54]
Carbon-coated CNT@Fe$_2$O$_3$	LIBs	NA	NA	≈800	500	75%/100	[55]
Fe$_3$O$_4$@N-C	LIBs	NA	NA	1063	1000	98.4%/1000	[58]
Fe$_3$O$_4$@GS/GF	LIBs	NA	NA	1059	93	80%/150	[60]
Fe$_3$O$_4$-C nanospindles	LIBs	NA	NA	530	462	70%/80	[63]
Fe$_3$O$_4$@C@PGC	LIBs	NA	NA	998	1000	97%/100	[64]
3D porous γ-Fe$_2$O$_3$@C	SIBs	0.6	1.0	740	200	38%/200	[67]
Fe$_2$O$_3$	SIBs	NA	NA	386	100	41%/200	[68]
Fe$_3$O$_4$@C	SIBs	0.75	1.0	309	500	36%/100	[70]
Fe$_3$O$_4$@C/rGO	SIBs	NA	NA	306	100	44%/100	[73]
Fe$_2$O$_3$@NC	SIBs	≈1.5	≈1.875	473.7	100	>100%/100	[74]
γ-Fe$_2$O$_3$/PCF	LIBs SIBs	1.5	NA	980 291	100 100	97%/100 78%/50	[75]
S-Fe$_2$O$_3$	SIBs	0.4	NA	367	5000	91%/200	[76]

relatively low energy storage efficiency; (ii) the wide operational voltage range to obtain high capacity values, limiting the overall energy density of the resulting full-cells, which would eventually provide significantly varying output voltages.

3.2. Cobalt Oxide (CoO, Co$_3$O$_4$)

Also the cobalt oxides CoO and Co$_3$O$_4$ have attracted great attention as potential electrode active materials due to their advanced redox properties. As an anode material in LIBs, CoO can deliver a high theoretical specific capacity (716 mAh g^{-1}) according to the reaction: CoO + 2Li$^+$ + 2e$^-$ ⇄ Co + Li$_2$O. As an example, Cao and co-workers[77] fabricated CoO nanowire (NW) clusters (NWCs) consisting of ultrasmall nanoparticles (≈10 nm) following a hydrothermal synthesis method. These nanowires were directly grown on the copper current collector. At a dis/charge rate of 1 C (i.e., 716 mA g^{-1}), the resulting electrode delivered a high capacity of 1516 mAh g^{-1}, which was almost maintained (≈1331 mAh g^{-1}) even at 5 C. Passerini and co-workers[42] fabricated a CoO-Co-C nanocomposite via the in situ carbothermal reduction of Co$_3$O$_4$. When compared with the original Co$_3$O$_4$ nanoparticles, the CoO-Co-C composite showed enhanced long-term cycling stability and CE. Based on an in situ X-ray diffraction (XRD) analysis, they found that the metallic cobalt remains electrochemically inactive within the composite, while the obtained specific capacity is mainly derived from the comprised CoO. The authors reported that

the metallic cobalt enhanced the electronic conductivity of the composite electrode, but, unfortunately, had a negative effect on the long-term cycling performance by catalytically inducing the electrolyte continuous decomposition (**Figure 4**a–f).

Despite these promising studies for CoO, Co$_3$O$_4$ has been investigated far more extensively, since it possesses a markedly higher theoretical capacity (890 mAh g^{-1}) and is easier to prepare. Almost any cobalt salt, such as hydroxides, carbonates, nitrates, oxalates, acetates, or sulfates, generates Co$_3$O$_4$ above 300–400 °C heat treatment in air. Li and co-workers,[78] e.g., reported Co$_3$O$_4$ nanotubes synthesized using an anodic aluminum oxide (AAO) template, which exhibited very high cycling stability when compared with Co$_3$O$_4$ nanorods and nanoparticles. Chen and co-workers[79] reported a facile method to fabricate a composite of Co$_3$O$_4$ NPs (30–40 nm) embedded in electrically conductive graphene. When tested as anode active material for LIBs, the Co$_3$O$_4$/graphene electrode exhibited a reversible capacity of 935 mAh g^{-1} after 30 cycles, remarkable cycling stability with high CE (above 98%), and good rate performance. Lou et al.[80] reported a facile self-supported topotactic transformation method for the synthesis of needle-like Co$_3$O$_4$ nanotubes. The as-prepared Co$_3$O$_4$ nanotubes showed ultrahigh capacity of 918 mAh g^{-1} at 50 mA g^{-1} after 30 cycles. Similarly, Li et al.[81] reported mesoporous Co$_3$O$_4$ NW arrays, exhibiting high capacity and good rate performance, thus, being capable of retaining 50% of the initial capacity when increasing the dis/charge rate to 50 C. Yan et al.[82] further modified such 1D morphologies and developed C-doped Co$_3$O$_4$

ADVANCED
SCIENCE NEWS

www.advancedsciencenews.com

ADVANCED
ENERGY
MATERIALS

www.advenergymat.de
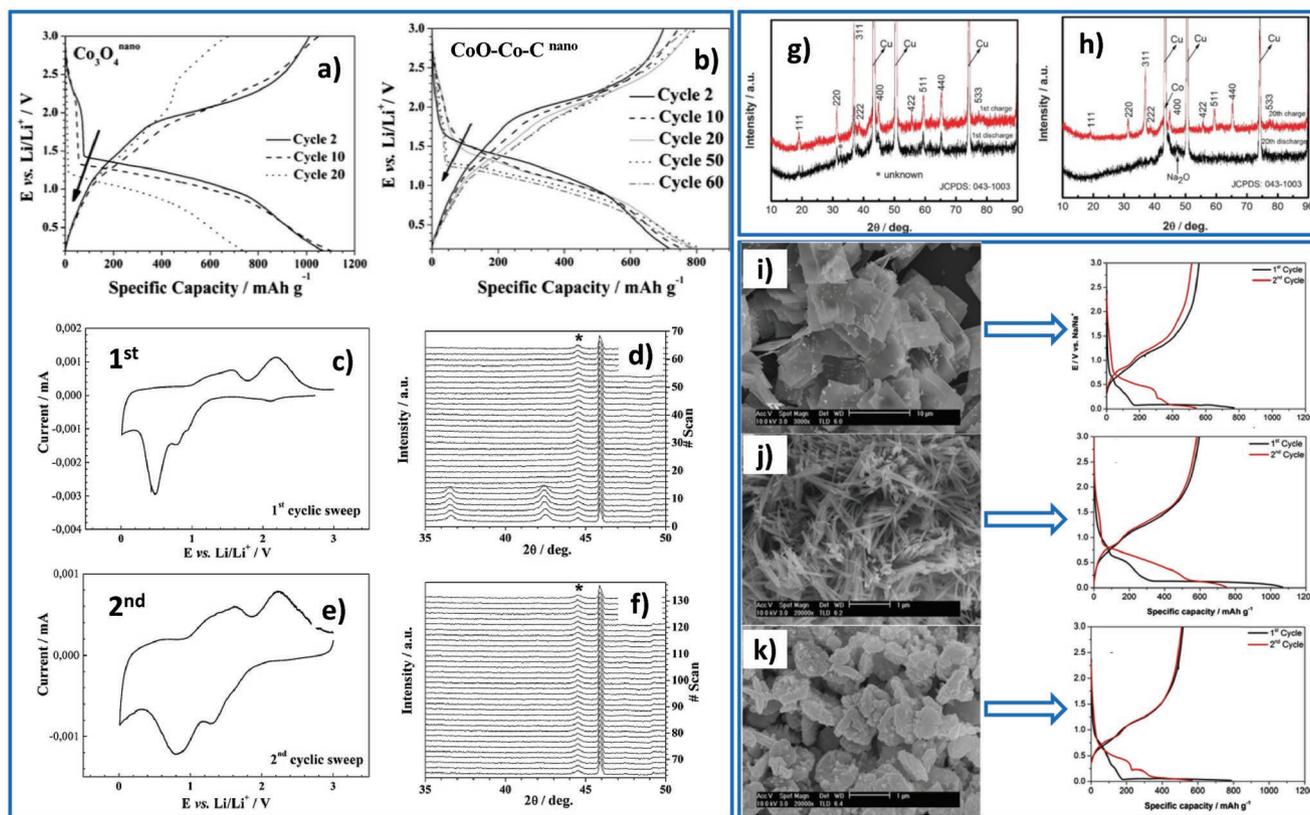
Figure 4. a,b) Selected dis/charge profiles for nanoparticulate Co_3O_4 and CoO-Co-C, revealing a better cycling stability for the latter, and c–f) an in situ XRD analysis of such CoO-Co-C nanocomposite: The corresponding first and second cyclic voltammogram and the simultaneous evolution of the XRD pattern. Reproduced with permission.[42] Copyright 2014, Wiley. g,h) Ex situ XRD patterns of Co_3O_4 electrodes in the fully discharged and charged states during the 1st and 20th cycle. Reproduced with permission.[82] Copyright 2014, Royal Society of Chemistry. i–k) SEM images of Co_3O_4 particles with different morphologies and the corresponding dis/charge profiles. Reproduced with permission.[88] Copyright 2016, Elsevier.

hollow nanotubes. Such heterogeneous doping was reported to generate a local built-in electric field due to an unbalanced charge distribution, which greatly facilitates the charge transfer. As a consequence, these Co_3O_4 hollow nanotubes (HNTs), assembled out of less than 10 nm nanocrystals benefitting from a "surface locking" effect and in situ topotactic conversion, demonstrated remarkable lithium uptake reversibility and a capacity of 950 mAh g^{-1} after 300 cycles at 500 mA g^{-1}.

The reversible capacity of cobalt oxides in Na-configuration is much lower than their theoretical capacity and the capacities obtained as Li-ion hosts. Rahman et al.,[83] by using of ex situ XRD and cyclic voltammetry experiments, proposed that the mechanism for the reversible conversion reaction of Co_3O_4 with Na would be: $Co_3O_4 + 8Na^+ + 8e^- \rightarrow 4Na_2O + 3Co$. According to the XRD analysis, after the 1st and 20th cycle, the conversion reaction is not completed in the first lithiation to 0.01 V, but progresses upon cycling. Nonetheless, the capacity maintained at 447 mAh g^{-1} after 50 cycles with about 86% capacity retention (Figure 4g,h). In another study, monodispersed hierarchical Co_3O_4 spheres intertwined with carbon nanotubes, thus, forming a Co_3O_4@CNTs hybrid, showed good cycling performance and rate capability with a capacity of up to 230 and 184 mAh g^{-1} at 1600 and 3200 mA g^{-1}, respectively.[84] A binder-free hierarchical CoO active materials grown on carbon nanofibers (CNFs) has been synthesized by Jiang et al.[85] They

achieved an improved electrochemical performance by controlling the amount of CoO in the CNFs. However, the capacity remained rather low with 193 mAh g^{-1} at 50 mA g^{-1} after 50 cycles. In fact, the CoO particles appeared rather large with a size of about 5 µm and highly aggregated. Some of them lost the contact with the CNFs, which presumably led to further performance deterioration. Such issue was prevented by Li et al.[86] when fabricating a Ti-doped CoO@C composite by annealing a Co-Ti MOF precursor. The Ti-doping and the porous carbon matrix enabled high electronic conductivity, thus, contributing to a fast electron transfer and mass transport. The composite electrode delivered a capacity of 285 mAh g^{-1} at 100 mA g^{-1} after 100 cycles. Similarly, Ding and co-workers reported MOF-derived 2D networks of CoO and N-doped CNT (CoO-NCNT) as anode material for LIBs and SIBs. This composite showed an excellent cycling performance with a capacity of about 580 and 450 mAh g^{-1} at a specific current of 0.5 A g^{-1} after 2000 and 300 cycles, respectively. Comparable sodium storage capacity was reported by Xu et al.[87] for Co_3O_4 nanoparticles confined in rambutan-like hollow carbon spheres. The material revealed a high capacity of 409 mAh g^{-1} after 500 cycles at 0.5 A g^{-1}, corresponding to a capacity retention of 74.5%. When paired with a $Na_{0.5}MnO_2$ cathode, the resulting sodium-ion full-cell delivered a capacity of 514 mAh g^{-1} at 0.1 A g^{-1} based on the anode mass loading. Generally, these studies demonstrate

ADVANCED
SCIENCE NEWS
www.advancedsciencenews.com

ADVANCED
ENERGY
MATERIALS
www.advenergymat.de

Table 3. Overview of reported electrochemical performances for selected cobalt oxide-based active materials and composites.

Materials	LIBs or SIBs	Active material mass loading [mg cm^{-2}]	Composite material loading [mg cm^{-2}]	Specific capacity [mAh g^{-1}]	Specific current [mA g^{-1}]	Capacity retention (based on charge capacity)/number of cycles	Ref.
CoO-Co-C	LIBs	2.2–2.4	NA	800	44.5	87.5%/80	[42]
Co$_3$O$_4$ nanotubes	LIBs	NA	NA	500	50	58.8%/100	[77]
Co$_3$O$_4$/graphene	LIBs	NA	NA	≈935	50	>100%/30	[78]
Needle-like Co$_3$O$_4$ nanotubes	LIBs	NA	NA	918	50	97%/30	[79]
Co$_3$O$_4$NW arrays	LIBs	NA	NA	700	111	NA	[80]
C-doped Co$_3$O$_4$ HNTs	LIBs	1	1.25	950	500	NA	[81]
Nanostructured Co$_3$O$_4$	SIBs	NA	NA	447	25	85%/50	[82]
Co$_3$O$_4$@CNTs	SIBs	0.8	1	487	NA	47%/20	[83]
CNF/CoO-4	LIBs SIBs	NA	NA	530 193	200 50	NA	[84]
ZnO-Co$_3$O$_4$@CC	LIBs SIBs	1.5–1.7	NA	1785 684	200 200	NA	[85]
Ti-doped CoO@C	LIBs SIBs	1–1.5	1.42–2.14	1108 285	200 100	>100%/150 ≈100%/100	[86]
CoO-NCNTs	LIBs SIBs	1.05	1.5	583 450	500	87.4%/2000 86.8%/2000	[87]
Co$_3$O$_4$	SIBs	0.5–1	0.67–1.33	500	89	NA	[88]

the advantageous effects of designing tailored (hierarchical) composites to achieve improved cycling stability and rapid electrode kinetics. Investigating the impact of the active material particle shape itself, Longoni et al.[88] synthesized Co$_3$O$_4$ with different morphologies and found that the electrochemical properties strongly are affected by the particle morphology. According to their results, a needle-like morphology allows for the realization of high specific capacities, exceeding 500 mAh g^{-1} after 50 cycles. In addition to their findings of this morphology–performance correlation, the authors unveiled that the reconversion proceeds only to the CoO phase, instead of the fully oxidized one, i.e., Co$_3$O$_4$. Further, they demonstrated that the CoO phase is more stable than Co$_3$O$_4$ during the charge/discharge process (Figure 4i–k) and presented a presodiation treated electrode for conversion materials, sensibly decreasing the first cycle irreversibility and improving the cyclability. The findings of the studies reviewed herein are comparatively summarized in **Table 3**. Generally, cobalt oxides are probably the most advanced conversion-type electrode materials thanks to the high reversibility of the conversion reaction, accompanied by high specific capacities. The use of large amounts of cobalt, however, essentially excludes any reasonable application in commercial cells for cost, abundance, and toxicity issues. Besides, as for iron oxides, the main hurdle still remains: the large voltage hysteresis and the wide operational potential range. Nonetheless, the extensive work on cobalt oxides published already may render this material a good choice for a suitable model compound in order to better understand the underlying mechanisms.

3.3. Manganese Oxide (MnO, Mn$_3$O$_4$, MnO$_2$)

Compared with other TMOs, manganese oxide is an attractive anode material due to its abundancy in the earth's crust,

low redox potential, relatively low polarization, high theoretical capacity, and environmental friendliness. However, manganese oxides are commonly affected by poor cyclability as a result of the large volume changes during the conversion reaction and the low electronic conductivity, both degrading the electrochemical performance. Therefore, improving the mechanical strength and electronic conductivity of manganese oxide-based electrodes is essential. An N-doped, cauliflower-like porous MnO@C/N composite prepared through a one-pot hydrothermal reaction, for example, showed good electrochemical performance as anode material for both LIBs and SIBs.[89] When employed as Li host, the material retained a capacity exceeding 830 mAh g^{-1} after 300 cycles at 500 mA g^{-1}. For SIBs, the reversible capacity was much lower. In fact, only 123 mAh g^{-1} were achieved after 200 cycles at 0.1 A g^{-1}. In a different approach, Huang and co-workers[90] synthesized MnO nanoparticles encapsulated in 3D mesoporous interconnected carbon networks (3D MnO-MICN) via a microwave-polyol process. When studied as anode active material for LIBs, the 3D MnO-MICN nanocomposite exhibited a highly reversible capacity above 1220 mAh g^{-1} and an average CE of ≈99% for more than 200 cycles at a specific current of 0.2 A g^{-1}. Chu et al.[91] reported MnO@Mn$_3$O$_4$ nanoparticles embedded in an N-doped porous carbon framework (NPCF) derived from Mn-organic clusters (MnO@Mn$_3$O$_4$/NPCF). Such composite displayed an excellent lithium-storage performance (1500 mAh g^{-1} at 0.2 A g^{-1} after 270 cycles), though a detailed analysis indicated that this high capacity essentially originated from capacitive Li$^+$ accumulation. Additionally, first-principle calculations revealed that a strong polarization and electronic interaction existed at the interfaces in the Mn$_3$O$_4$/NPCF composite, which effectively strengthen the interaction between the MnO@Mn$_3$O$_4$ nanoparticles and the NPCF. Meanwhile, the presence of defects in NPCF decreased the diffusion barrier, thus, enhancing the pseudocapacitive Li$^+$ storage, leading to

ADVANCED
SCIENCE NEWS
www.advancedsciencenews.com

ADVANCED
ENERGY
MATERIALS
www.advenergymat.de
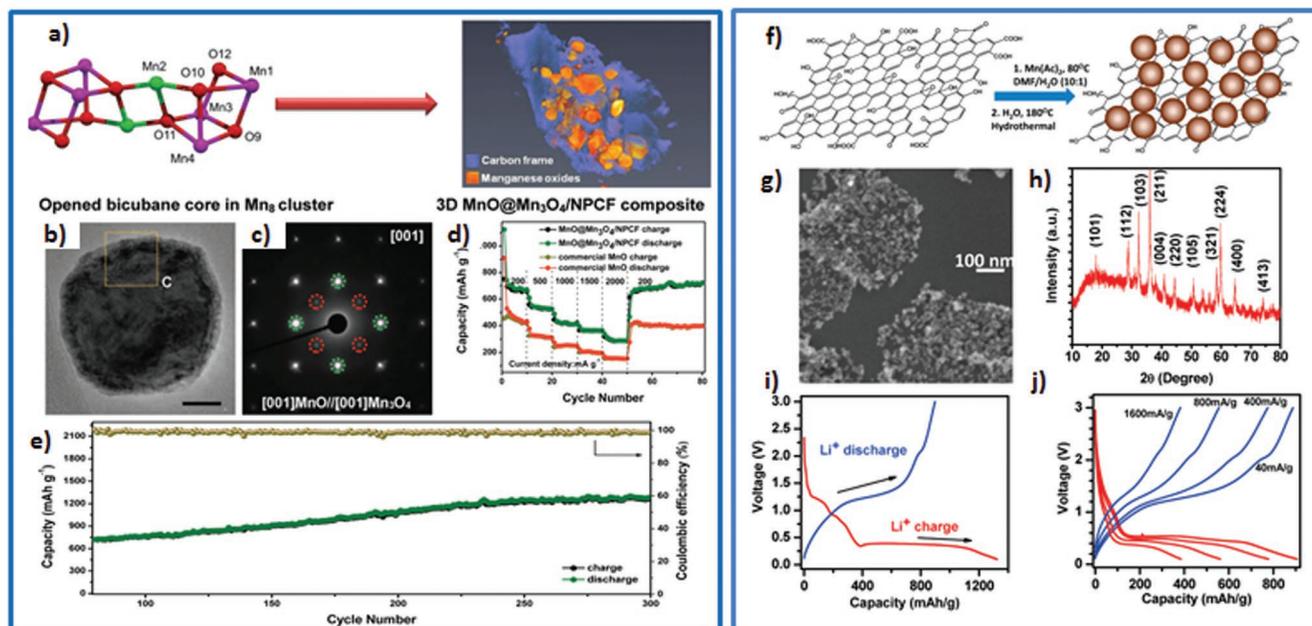
Figure 5. a) Schematic illustration of the synthesis process of the MnO@Mn$_3$O$_4$/NPCF composite; b,c) TEM image of a single MnO@Mn$_3$O$_4$ and the corresponding SAED pattern; d,e) Rate capability and long-term constant current cycling performance. Reproduced with permission.[91] Copyright, Wiley. f) Schematic presentation of the two-step synthesis of Mn$_3$O$_4$/rGO: g,h) The corresponding SEM image and XRD pattern of such Mn$_3$O$_4$/rGO hybrid; i,j) The dis/charge profiles for the first cycle and at varying specific currents. Reproduced with permission.[94] Copyright 2010, American Chemical Society.

higher reversible capacities and an enhanced long-term cycling stability (**Figure 5**a–e). Diao et al.[92] developed bicomponent (FeO)$_x$(MnO)$_{1-x}$ encapsulated in an amorphous carbon matrix as negative active material for LIBs. The authors controlled the calcination temperature of the precursor to tune the bicomponent compound with varying stoichiometry. The thus optimized (FeO)$_{0.198}$(MnO)$_{0.802}$, obtained at 800 °C, displayed the best performance, which they assigned to optimized electronic interactions between the single TMOs FeO and MnO as well as the carbon matrix. Good electrochemical performance has also been reported for coaxial manganese oxide/CNT arrays (MnO$_2$/CNT), which had been synthesized by using porous alumina as the template.[93] The highly conductive CNT core offers enhanced electron transport to the MnO$_2$ shell and effectively buffers the occurring volume changes. Employing reduced graphene oxide (rGO) instead of CNTs, Dai and co-workers[94] reported a two-step solution-phase method for fabricating Mn$_3$O$_4$/rGO. This composite showed an unprecedented high capacity (≈900 mAh g^{-1}), based on the mass of Mn$_3$O$_4$, as well as good rate capability and cycling stability (Figure 5f–j). Similarly, N-doped carbon-coated MnO embedded in graphene ribbons (IGR-MnO-C) showed good cycling stability and high reversible lithium storage capacity.[95] Xiao et al.[96] synthesized yolk–shell MnO@C nanodiscs via a carbothermal reduction process. The in situ formed void space allows for buffering the occurring volume changes of MnO and the uniform carbon shell improved the electronic conductivity. As a result, such yolk–shell MnO@C displayed excellent cycling stability and high reversible capacity with 605 mAh g^{-1} after 600 cycles at 1 A g^{-1}. Focusing on the structure of the manganese oxide itself rather than the incorporation of secondary electronically conductive phases, Abruna

and co-workers[97] synthesized sponge-like nanosized Mn$_3$O$_4$ as Li-ion host. The initial reversible capacity was 869 mAh g^{-1} with a first cycle CE of 65%. Even after 40 cycles, a high reversible capacity of ≈800 mAh g^{-1} was achieved.

Similarly, Weng et al.[98] developed a novel approach to prepare void-confined ultrasmall MnO$_2$ using porous SiO$_2$ as sacrificial template. The resulting material was characterized by a flake-like morphology with a flake width of several hundred nanometers. Electrodes based on these MnO$_2$ flakes exhibited a high reversible capacity of 570 mAh g^{-1} as sodium host and a capacity retention of about 70% after 500 cycles when applying a specific current of 150 mA g^{-1}. Based on an in situ X-ray absorption near-edge spectroscopy (XANES) study, the authors showed that the electrochemical reaction occurs via a two-phase conversion reaction, i.e., (Mn(III)-O$_{1.5}$ + Na$^+$ + e$^-$ ⇌ 1/2Na$_2$O + Mn(II)-O) and non-Mn-centered redox reactions, such as the formation of a polymer-like film, surface space-charge layer, etc. (**Figure 6**a–f).

Porous MnO@C nanorods were synthesized via carbonization of a Mn-based MOF precursor. This MnO@C hybrid exhibited a reversible capacity of 260 mAh g^{-1} after 100 cycles at a specific current of 50 mA g^{-1}.[99] Li et al.[100] reported feather-like MnO$_2$ grown on carbon paper by a hydrothermal method and applied this composite as negative active material for SIBs, providing a rather high reversible capacity of 300 mAh g^{-1} after 400 cycles at 0.1 A g^{-1}. Peng and co-workers[101] synthesized ultrafine MnO nanoparticles, with a particle size of 4 nm, anchored on nitrogen-doped CNTs (NDCT@MnO) as anode active material for SIBs. They found that the structure and the Na-storage behavior of the resulting nanocomposites was highly influenced by the carbonization temperature. The composite provides high rate capability
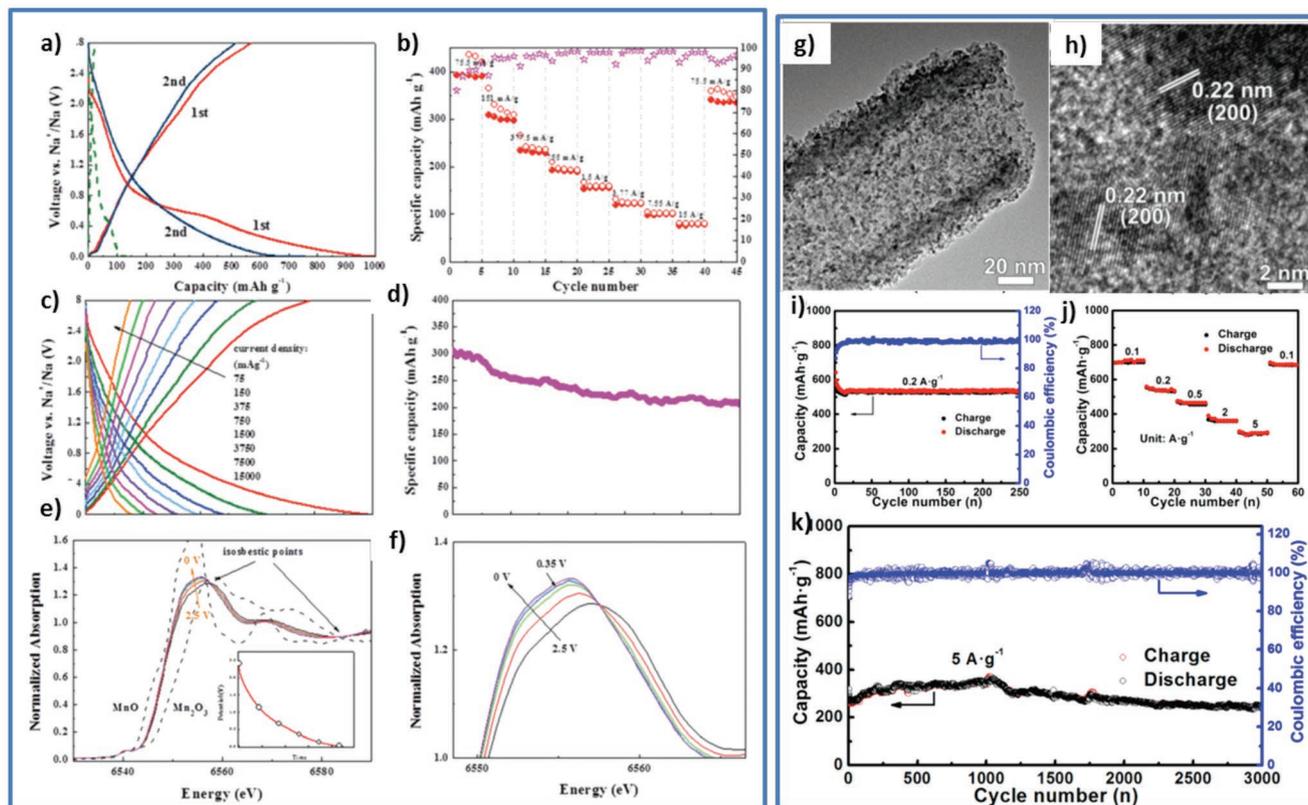
Figure 6. a–d) Electrochemical performance of ultrafine MnO_2 flakes as active material for SIBs, including the dis/charge profiles, rate capability, and long-term constant current cycling. e,f) Operando synchrotron XANES spectra acquired during the second discharge (inset) of the ultrafine-MnO_2 electrode. Reprinted from ref. [98] with permission from The Royal Society of Chemistry. g,h) TEM and HRTEM images of NDCT@MnO. i–k) Electrochemical performance of NDCT@MnO. Reproduced with permission.[101] Copyright 2017, American Chemical Society.

and long-term cycling performance. In particular, the composite showed a reversible specific capacity (709 mAh g^{-1} at a specific current of 0.1 A g^{-1}) and high capacity retention of 536 mAh g^{-1} after 250 cycles at 0.2 A g^{-1}. Even at higher specific currents (5 A g^{-1}), a capacity of 273 mAh g^{-1} was retained after 3000 cycles (Figure 6g–k). **Table 4** comparatively

Table 4. Overview of reported electrochemical performances for selected manganese oxide-based active materials and composites.

Materials	LIBs or SIBs	Active material mass loading [mg cm^{-2}]	Composite material loading [mg cm^{-2}]	Specific capacity [mAh g^{-1}]	Specific current [mA g^{-1}]	Capacity retention (based on charge capacity)/number of cycles	Ref.
MnO@C/N	LIBs	NA	NA	837	500	>100%/300	[89]
	SIBs			123	100	91.1%/200	
MnO-MICN	LIBs	NA	NA	1224	200	NA	[90]
MnO@Mn$_3$O$_4$/ NPCF	LIBs	1 ± 0.2	NA	1500	200	>100%/300	[91]
FMO-800	LIBs	≈0.6	≈0.75	1523	200	119%/300	[92]
MnO$_2$/CNT	LIBs	NA	NA	500	50	NA	[93]
Mn$_3$O$_4$/RGO	LIBs	NA	NA	≈900	40	NA	[94]
IGR-MnO-C	LIBs	≈1	≈1.25	904	500	>100%/500	[95]
MnO@C-YS	LIBs	≈1	≈1.42	605	1000	111%/600	[96]
Mn$_3$O$_4$	LIBs	NA	NA	800	30	92%/40	[97]
UF-MnO$_2$	SIBs	NA	NA	567	150	>70%/ 500	[98]
MnO@C	SIBs	NA	NA	260	50	46.7%/100	[99]
MnO$_2$/CP	SIBs	≈2	NA	≈300	100	63%/400	[100]
NDCT@MnO-7	SIBs	0.8	NA	536	200	≈100/250	[101]

**ADVANCED
SCIENCE NEWS**

www.advancedsciencenews.com

**ADVANCED
ENERGY
MATERIALS**

www.advenergymat.de

summarizes the findings of the herein reviewed studies on manganese oxides. In fact, given that the general issues of conversion-type materials (voltage hysteresis, limited cycle life, etc.) and the relatively low electronic conductivity of such materials might be overcome, manganese oxides would be an ideal candidate for commercial applications thanks to the high abundance, low cost, environmental friendliness, and biocompatibility of manganese. Moreover, manganese oxide shows the lowest de/lithiation/sodiation potentials within a rather narrow voltage range, favoring energy density and stable output voltages on the full-cell level. Especially for sodium storage, though, the capacity retention is still too low and the cycle life is rather limited. Consequently, the detailed reaction mechanism and the underlying thermodynamics and kinetics remain to be elucidated particularly for sodium battery applications.

3.4. Copper Oxide (Cu_2O, CuO)

Copper oxides, Cu_2O and CuO, are promising conversion-type anode materials due to their environmentally benignity and reversible theoretical capacities of 375 and 674 mAh g^{-1}, respectively. Studies on Cu_xO in various morphologies have been reported. Spherical and phase-pure CuO nanoparticles were synthesized by the controlled pyrolysis of Cu-based MOFs, as reported by Banerjee et al.[102] Similarly, Chen and co-workers[103] fabricated CuO/Cu_2O composite hollow polyhedrons from Cu-based MOFs. CuO hollow nanocubes have been synthesized by a controlled oxidation reaction of Cu_2O nanocubes.[104] Unique Cu_2O-CuO-TiO_2 hollow nanocages were synthesized via a self-templated hydrothermal method.[105] The large void space in this material could solve the critical volume expansion issue during the charge/discharge cycles, although it reduces the volumetric capacity. As anode materials for LIBs, the fabricated Cu_2O-CuO-TiO_2 hollow nanocages exhibited superior reversible capacity (700 mAh g^{-1} at 50 mA g^{-1}) for over 80 cycles. In a slightly different approach, combining two different conversion materials, 3D hierarchical Co_3O_4/CuO NW heterostructure arrays have been successfully fabricated based on CuO NW arrays directly grown on Ni foam (**Figure 7**a–e), which are further evaluated as carbon- and binder-free electrodes for high-performance LIBs. When compared with the single Co_3O_4 nanosheets and CuO NWs, these composites exhibited a synergistic effect with enhanced electrochemical performance, maintaining a specific capacity of 1191 mAh g^{-1} after 200 cycles at a specific current of 200 mA g^{-1}, corresponding to a capacity retention of 90.9%, which is higher than that of the single Co_3O_4 nanosheets, providing only 664 mAh g^{-1} after 100 cycles—just like the single CuO NWs with 554 mAh g^{-1} after 100 cycles.[106]

Following a comparably simple approach, nanocomposites with CNTs or graphene have been investigated to attain a stable cycling performance.[107,108] For instance, a ternary Cu_2O/CuO/rGO composite with a 3D hierarchical nanostructure was fabricated by a hydrothermal method. The electrochemical reaction mechanism of this composite was studied by in situ Raman spectroscopy. The characteristic Raman peak of CuO becomes less intense upon reduction, indicating that CuO transforms to Cu_2O and Cu. Upon reoxidation, the characteristic peak

gradually increases, which supports the (partial) reversibility of the conversion process (Figure 7f–k).[109]

The employment of copper oxide based anodes in lithium-ion full-cells has been investigated inter alia by Verrelli et al.[110,111] In a CuO-MCMB/$LiNi_{0.5}Mn_{1.5}O_4$ full-cell, ≈110 mAh g^{-1} was achieved after 100 cycles at a specific current of 148 mA g^{-1} and the gravimetric energy density was 420 Wh kg^{-1}. When using $Li_{0.85}Ni_{0.46}Cu_{0.1}Mn_{1.49}O_4$ as the cathode, the battery operates for over 50 cycles at a specific current of 48.7 mA g^{-1} with an average voltage of 3.4 V and a stable capacity of 100 mAh g^{-1}.[111] These full-cells showed good cycling stability and remarkable rate capability. When combining such anodes with an ionic liquid-based electrolyte, the CuO-MCMB electrode delivered a high capacity of 580 mAh g^{-1} with a CE exceeding 98%. For the full-cell, comprising a $LiNi_{0.5}Mn_{1.5}O_4$ cathode, the use of the ionic liquid electrolyte resulted in a full-cell with an average operating voltage of 3 V and specific capacity about 120 mAh g^{-1}.[112] However, the cycling performance and voltage-profile retention remained limited. To address these issues, the authors further modified the conversion-type electrode material by combining CuO and Fe_2O_3 in the composition. Such a mixed conversion anode coupled with a spinel $Li_{1.35}Ni_{0.48}Fe_{0.1}Mn_{1.72}O_4$ cathode eventually allowed for a substantially enhanced full-cell performance.[113] The working voltage of the cell was 3.6 V and a capacity of 110 mAh g^{-1} was achieved after 100 cycles at specific current of 148 mA g^{-1} with an average CE of more than 99%. In another study on lithium-ion full-cells, Zhang et al.[114] combined a CuO nanorod array anode and a high-voltage spinel $LiNi_{0.5}Mn_{1.5}O_4$ cathode. These full-cells exhibited good cycling performance (84% capacity retention after 100 cycles at 0.5 C) and good rate performance (≈240 mAh g^{-1} at 10 C; 1 C = 674 mA g^{-1}).

Following these promising results, copper oxides were also investigated for sodium-ion applications. Flexible and porous CuO nanorod arrays (CNAs), for example, synthesized by simply etching commercial Cu foils, were used as binder-free anodes for SIBs, delivering a specific capacity of 291 mAh g^{-1} after 450 cycles at 200 mA g^{-1} and a capacity retention of 45.2%.[115] Similarly, N-doped carbon-coated CuO nanorod arrays (NC-CuO) were grown on Cu net to realize freestanding electrodes for both LIBs and SIBs.[116] For SIBs, the NC-CuO-based electrodes provided a reversible capacity of 214.97 mAh g^{-1} after 100 cycles at a specific current of 0.5 A g^{-1}, benefitting from the extensive space between the single CuO nanorods and the carbon coating surface layer, which enabled high structural stability and electronic conductivity. In a very comparable study, Ni et al.[117] reported CuO nanoarrays grown on 3D Cu foam. Instead of applying a carbon coating, however, they deposited TiO_2 thin films on the CuO surface by atomic layer deposition (R-CuO), with the goal to decrease the volume variation upon de/sodiation. As a matter of fact, the resulting R-CuO electrodes showed good cycling performance and excellent rate capability (306 mAh g^{-1} after 200 cycles at 1.2 A g^{-1} and 155 mAh g^{-1} after 1000 cycles at 3.0 A g^{-1}). When coupled with $Na_{0.67}(Ni_{0.23}Mg_{0.1}Mn_{0.67})O_2$ as cathode active material, the resulting full-cell delivered a specific energy of 142 Wh kg^{-1}. Liu et al.[118] found that the surface coating with carbon and Au allows for controlling the elongation rate of the nanowires along the ⟨110⟩ growth direction and for increasing
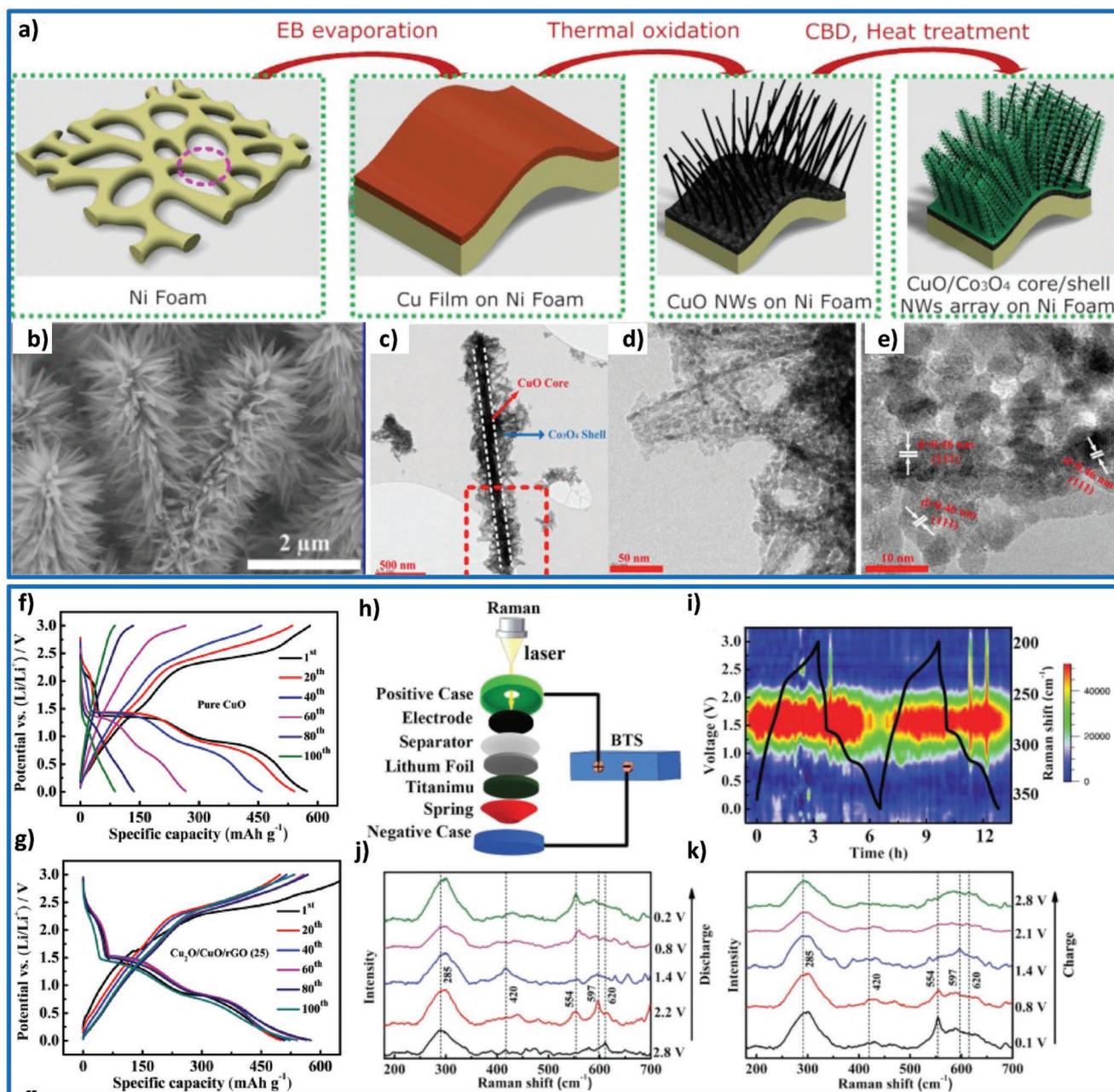
Figure 7. a) Schematic illustration of the fabrication procedure of CuO/Co$_3$O$_4$ core/shell heterostructure nanowire arrays. b) SEM and c–e) TEM images of such CuO/Co$_3$O$_4$ core/shell nanowires. Reproduced with permission.[106] Copyright 2014, Elsevier. f,g) Discharge and charge profiles of electrodes based on CuO and Cu$_2$O/CuO/rGO for selected cycles. h) Setup for the in situ Raman analysis of the ternary Cu$_2$O/CuO/rGO composite with i) the resulting 2D Raman data including the dis/charge profiles and the transformed 1D spectra for the j) discharge and k) charge process. Reproduced with permission.[109] Copyright 2018, Wiley.

the electrochemical reaction kinetics, which then led to an enhanced sodium storage performance. These results highlight the significant impact of surface coatings on the electrochemical performance. Additionally, according to an in situ transmission electron microscopy (TEM) characterization, the authors observed that the electrochemical conversion of CuO is partially irreversible: Part of the Cu that is formed during the sodiation remains upon desodiation, while both oxide phases, i.e., CuO and Cu$_2$O, were detected, which explains at least part

of the large initial capacity loss. Wang et al.[119] reported porous CuO nanowires as anode for SIBs with a first cycle sodiation capacity of 640 mAh g^{-1} (at 50 mA g^{-1}) and maintaining and 303 mAh g^{-1} after 50 cycles. Based on an ex situ characterization, the authors proposed that, upon sodiation, Na$^+$ ions are inserted into CuO to form Cu$_2$O and Na$_2$O. In a second step, Cu$_2$O decomposes into Cu nanoparticles embedded in the Na$_2$O matrix. During the desodiation process, Cu nanoparticles are first oxidized to form Cu$_2$O and then converted back to CuO.

ADVANCED
SCIENCE NEWS
www.advancedsciencenews.com

ADVANCED
ENERGY
MATERIALS
www.advenergymat.de
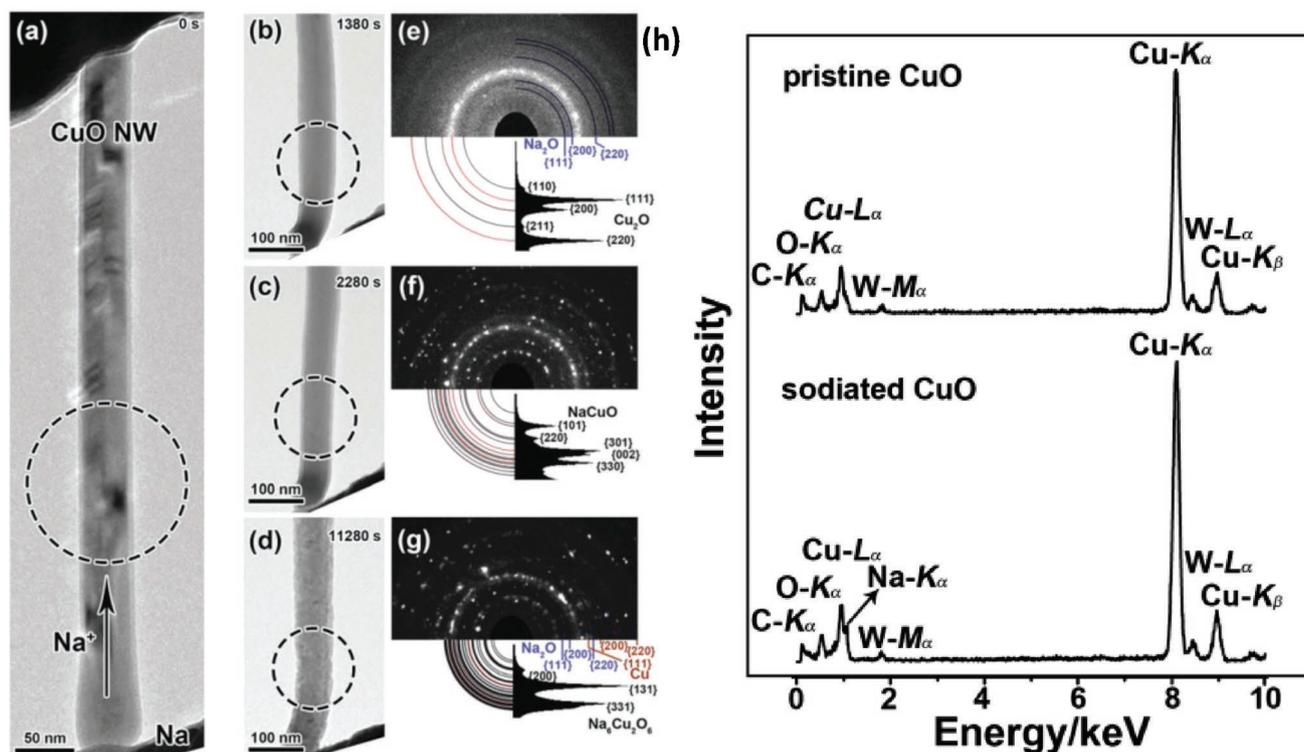
Figure 8. a) TEM image of a pristine CuO NW. b–d) TEM images of the sodiated CuO NW at different degrees of sodiation and the corresponding electron diffraction patterns of the circled area. h) EDX spectra of pristine and sodiated CuO NWs. Reproduced with permission.[120] Copyright 2015, Royal Society of Chemistry.

However, Liu et al.[120] proposed a rather different kinetic evolution of the morphology and phase conversion in CuO nanowires during sodiation (**Figure 8**). According to the in situ TEM investigation, the authors proposed that the eventual sodiation products of CuO were $Na_6Cu_2O_6$, Na_2O, and Cu according to the following reactions

$$2CuO + 2Na^+ + 2e^- \rightarrow Cu_2O + Na_2O \tag{4}$$

$$Cu_2O + Na_2O \rightarrow 2NaCuO \tag{5}$$

$$7NaCuO + Na^+ + e^- \rightarrow Na_6Cu_2O_6 + Na_2O + 5Cu \tag{6}$$
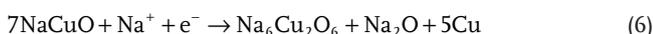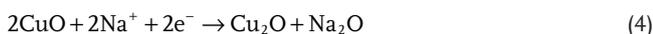
This discrepancy may originate from the different electrolytes used. In the latter work, in fact, a solid electrolyte was utilized instead of a liquid electrolyte. Further work is required to clarify whether different types of electrolytes may influence the sodiation process or if other parameters are affecting the reaction mechanism. Targeting to increase the electronic conductivity of the active material, Chen and co-workers[121] fabricated sub-micrometer CuO/C sphere-shaped particles by means of an aerosol spray pyrolysis. The CuO nanoparticles (≈10 nm) were uniformly embedded in the carbon matrix, which significantly enhanced the electronic conductivity of the composite and helped to buffer the volume variations of CuO during dis/charge. Based on the unique structure, the composite delivered a capacity of 402 mAh g^{-1} after 600 cycles at 200 mA g^{-1}. **Table 5**

provides a comparative summary of the findings reviewed herein on copper oxides. Just like manganese or iron oxides, they are characterized by nontoxicity and facile synthesis—though of much higher cost—and besides the high electronic conductivity of metallic copper, the corresponding oxides are essentially insulators. To address this issue, researchers have introduced CNTs or graphene as secondary phases and developed well-designed nanostructures like nanorods, nanowires, or hollow structures (see Table 5) to improve the performance. However, hollow structures generally result in low volumetric energy densities and the required (template-assisted) synthesis procedures are commonly complicated and, thus, costly. Moreover, the cycle life and capacity retention of copper oxide anodes remain improvable—also for lithium-ion anode applications. The development of effective strategies to improve the rate capability and cycling performance is needed.

3.5. Nickel Oxide (NiO)

Also NiO, a p-type wide bandgap semiconductor, has been considered as an attractive anode candidate for LIBs. The theoretical specific capacity of NiO is 718 mAh g^{-1} based on the reversible reduction of the oxide to metallic nickel and lithium oxide, i.e., $NiO + 2Li^+ + 2e^- \leftrightarrows Ni + Li_2O$.[122] Nevertheless, just as for other conversion-type anodes, the cycling stability and rate capability of NiO remain to be improved. To overcome these issues, for instance, 2D sheet-like nanoparticles were

**ADVANCED
SCIENCE NEWS**

www.advancedsciencenews.com

**ADVANCED
ENERGY
MATERIALS**

www.advenergymat.de

Table 5. Overview of reported electrochemical performances for selected copper oxide-based active materials and composites.

Materials	LIBs or SIBs	Active material mass loading [mg cm^{-2}]	Composite material loading [mg cm^{-2}]	Specific capacity [mAh g^{-1}]	Specific current [mA g^{-1}]	Capacity retention (based on charge capacity)/number of cycles	Ref.
Pure CuO nanoparticles	LIBs	5	6.5	210	2000	≈90%/40	[102]
CuO/Cu$_2$O hollow polyhedrons	LIBs	NA	NA	480	100	66%/248	[102]
CuO nanostructures	LIBs	NA	NA	560	150	>100%/50	[104]
Cu$_2$O-CuO-TiO$_2$	LIBs	NA	NA	700	50	58%/85	[105]
Co$_3$O$_4$/CuO	LIBs	NA	NA	1191	200	90.9%/200	[106]
CuO-CNT nanomicrospheres	LIBs	≈2.5	≈3.125	500	67	NA	[107]
CuO/CNT	LIBs	NA	NA	650	NA (0.1 C)	100%/100	[108]
Cu$_2$O/CuO/rGO	LIBs	NA	NA	550	500	NA	[119]
CuO-MCMB	LIBs	≈3.5	≈4.375	500–400	52	NA	[110]
CuO-MCMB	LIBs	0.8	1	400	50	77%/50	[112]
CuO-Fe$_2$O$_3$-MCMB	LIBs	1.6–2.8	2.0–3.5	500	120	NA	[113]
CuO nanorod array	LIBs	0.8	1	666	500	91%/100	[114]
CuO nanorod arrays	SIBs	≈2.0	NA	290.6	200	45.2%/450	[115]
NC-CuO array	LIBs SIBs	1.8	NA	551.66 214.97	500 500	>100%/200 NA	[116]
R-CuO nanoarray	SIBs	6	NA	155	3000	82%/1000	[117]
Porous CuO nanowires	SIBs	NA	NA	303	50	47.3%/50	[119]
10-CuO/C	SIBs	NA	NA	402	200	NA	[121]

synthesized, offering promising performance as anode material in LIBs. Vertically aligned NiO nanowalls[123] showed a reversible capacity of ≈638 mAh g^{-1} after 85 cycles at a specific current of 895 mA g^{-1} in the voltage range of 0.005–3.0 V versus Li. NiO-graphene sheet-on-sheet[124] nanostructures have been prepared and showed good cycling performance. After 40 cycles, at a specific current of 71.8 mA g^{-1}, a high reversible capacity of 1031 mAh g^{-1} was achieved, corresponding to a capacity retention of 97.6% with respect to the initial capacity. In consideration of the excellent electronic conductivity and mechanical flexibility of graphene, further studies, e.g., by Chen, and co-workers[125] found that NiO NSs strongly interact with graphene via a C—O—Ni bridge. According to their findings, this was the main reason for achieving higher reversible capacities and remarkable rate capability for such composites. Based on first-principle calculations, the oxygen bridges mainly derived from the interaction of epoxy/hydroxyl groups, present on graphene, and the Ni atoms of the NiO NSs. This intensive and strong interaction of Ni with oxygenated graphene was found to promote the rapid transition of electrons from graphene to NiO, thus, allowing for the enhanced reversibility of de/lithiation reaction. As a result, the NiO NS/graphene electrode showed high reversible capacity (883 mAh g^{-1} after 50 cycles at a specific current of 50 mA g^{-1}) and good rate performance. Introducing a second conversion-type transition metal oxide, Guo et al.[126] synthesized CuO@NiO ball-in-ball microspheres starting from Cu—Ni bimetallic organic frameworks. The resulting product displayed an elemental gradient (Cu-rich surface and Ni-rich core), matching the lithium reactivity sequence of the two metal oxides (CuO

and NiO). The composite showed a reversible, larger-than-theoretical capacity of 1061 mAh g^{-1}, and the capacity was fully maintained after 200 cycles. Using metallic nickel as precursor, Wang et al.[127] employed a low-temperature thermal oxidation of Ni foam to fabricate nanostructured NiO electrodes with excellent rate capability for high-power LIBs. The electrode achieved a capacity of more than 375 mAh g^{-1} at a dis/charge rate as high as 10 C. Moreover, the extensive void spaces in the electrode helped to buffer the huge volume changes during cycling.

Comparing the lithiation and sodiation mechanism and kinetics with a set of complementary experimental and theoretical techniques, He et al.[128] found that only the "shrinking-core mode" was observed during sodiation process. A passivation layer of Na$_2$O which formed at an early stage, starting from the outer particle surface, blocked the further sodiation and, thus, resulted in sluggish kinetics. Molecular dynamic simulation revealed that the sodiation pathway, leading to this shrinking-core mode, derives from a layer-by-layer reaction that occurs during sodiation. During the discharge process, however, the Li antisite defects will significantly distort the local NiO lattices, which facilitated the further insertion of and conversion with Li (**Figure 9**). In another direct comparison, Zou et al.[129] reported the preparation of a hierarchical NiO/Ni/graphene composite with a hollow ball-in-ball nanostructure, which revealed outstanding electrochemical performance as anode active material for both LIBs and SIBs (962 mAh g^{-1} after 1000 cycles at 2 A g^{-1} for LIBs and ≈200 mAh g^{-1} after 200 cycles at 200 mA g^{-1} for SIBs). The advantageous performance was assigned to the well-designed hierarchical hollow structure, which mitigates

ADVANCED
SCIENCE NEWS
www.advancedsciencenews.com

ADVANCED
ENERGY
MATERIALS
www.advenergymat.de
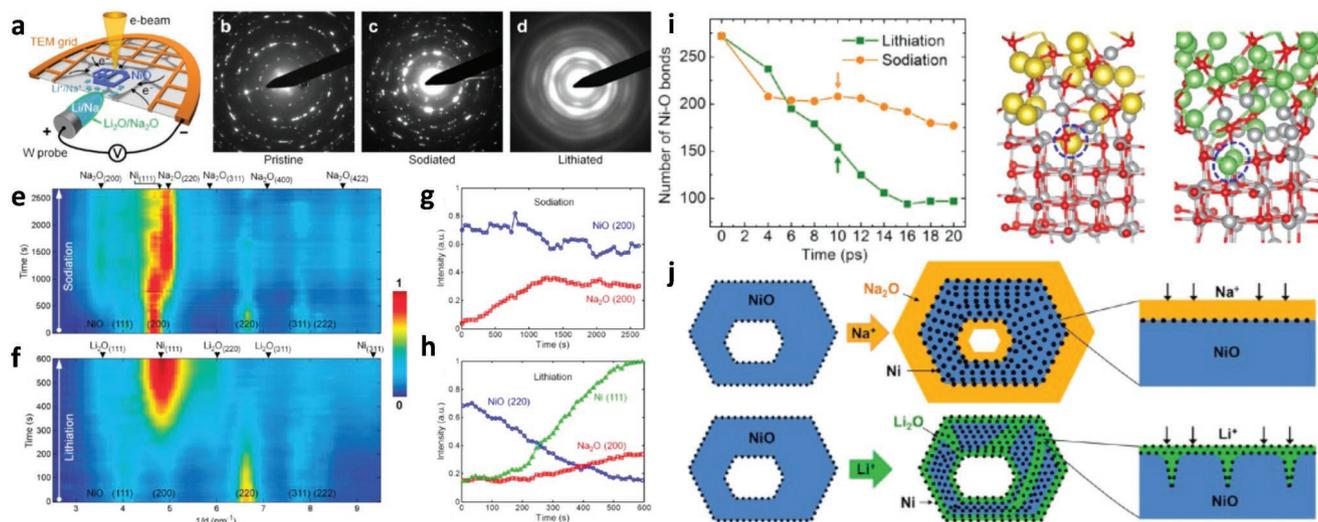
Figure 9. a) Schematic illustration of the in situ TEM setup: b–d) Electron diffraction patterns for the pristine, sodiated, and lithiated phase, e,f) colored intensity profiles as a function of reaction time for the sodiation and lithiation process, and g,h) the corresponding radial integration of the electron diffraction data as a function of time for the sodiation and lithiation with the Bragg peaks labeling. i) Ab initio MD simulations for the sodiation (in yellow) and lithiation (in green) of NiO. j) Schematic cartoons illustrating the different reaction modes for the electrochemical sodiation and lithiation. Reproduced with permission.[128] Copyright 2015, American Chemical Society.

the volume changes of NiO during cycling while the graphene matrix provides percolating electron-conductive pathways to facilitate charge transfer and enable the formation of a stable SEI. Another hierarchical hybrid structure has been prepared by Yang et al.,[130] constructing hollow Ni-NiO nanoparticles embedded in porous carbon nanosheets (Ni-NiO/PCNs). When testing this composite as anode material for SIBs, they recorded a specific capacity of 235 mAh g^{-1} after 5000 cycles at 1 A g^{-1}. The good electrochemical performance was attributed to the beneficial hollow core–shell structure and the high conductivity of the metallic Ni particles and carbon sheets, both providing continuous electron transfer pathways, which facilitates the electrochemical reaction kinetics. **Table 6** provides a summary of the findings reviewed herein. Generally, NiO has a kind of "intermediate" position in the list of conversion-type anode materials. The theoretical specific capacity of 714 mAh g^{-1} is higher than for copper oxides, but lower than for iron oxides, for instance. Nickel is not as costly as cobalt or copper, but more expensive than iron or manganese. Moreover, nickel is not as toxic as cobalt, but less biocompatible than iron or copper. It might provide high volumetric capacities thanks

to its high density of 6.67 g cm^{-3}, but suffers rather slow reaction kinetics; and while a variety of appealing strategies have been used to mitigate these issues, including the synthesis of very thin nanosheets or the incorporation of secondary carbon or metal oxide-based materials (see Table 6), the performance of NiO-based electrodes remains so far below expectation in terms of specific capacities and cycle life.

3.6. Ruthenium Oxide (RuO$_2$)

RuO$_2$ has a high theoretical capacity of 806 mAh g^{-1} and metallic-like conductivity. Nonetheless, its high price rules out any application in large-scale commercialized batteries. As one of the pioneers for the investigation of this material as active material in LIBs, Maier and co-workers[131,132] investigated the electrochemical reactivity with lithium over a wide voltage range from 0.05 to 4.3 V. They showed that this material can homogeneously and heterogeneously host lithium, offering a high capacity of 1130 mAh g^{-1} and extremely high first cycle CE of 98%. Based on ex situ Raman and XRD studies, they revealed

Table 6. Overview of reported electrochemical performances for selected nickel oxide-based active materials and composites.

Materials	LIBs or SIBs	Active material mass loading [mg cm^{-2}]	Composite material loading [mg cm^{-2}]	Specific capacity [mAh g^{-1}]	Specific current [mA g^{-1}]	Capacity retention (based on charge capacity)/number of cycles	Ref.
NiO nanowall	LIBs	0.1675	NA	≈638	895	≈98%/ 85	[123]
NiO-GNS	LIBs	NA	NA	1031	71.8	97.6%/40	[124]
NiONS/graphene composite	LIBs	1–2	1.25–2.25	1000	50	90%/50	[125]
CuO@NiO spheres	LIBs	≈1.6	≈2	1061	100	≈87%/200	[126]
NiO/Ni/graphene	LIBs	NA	NA	962	2000	>100%/1000	[129]
Ni-NiO/PCN	SIBs	NA	NA	235.4	1000	84.2%/5000	[130]

**ADVANCED
SCIENCE NEWS**
www.advancedsciencenews.com

**ADVANCED
ENERGY
MATERIALS**
www.advenergymat.de

that the Li storage in RuO_2 involves three reaction steps: (1) Ru/Li_2O nanocomposite formation, (2) Li-containing surface film formation, and (3) the interfacial deposition of Li within the Ru/Li_2O matrix. The cycling performance, however, remained stable only for the first three cycles in this voltage range, before it faded abruptly because of the large volume variation. In a later study, they found that amorphous nanosized RuO_2 offers enhanced performance compared with bulk crystalline RuO_2. As a case study, the open-circuit voltage of amorphous RuO_2 has an excess potential of 0.6 V in comparison with the potentials of crystalline RuO_2 with 60 nm and 10 µm sizes.[133] Nevertheless, to find out how far and in which way the quasi-amorphicity is kinetically linked with the electrochemical performance still requires further clarification. Gregorczyk et al.[134] used in situ TEM to investigate the reaction mechanism during the lithiation process of single-crystalline RuO_2 nanowires. They found that a large volume expansion about 95% occurred upon lithiation, and 26% remained irreversible, i.e., was not recovered after delithiation. Furthermore, they observed a noticeable surface roughening and lithium embrittlement, while the initial reaction from crystalline RuO_2 via an intermediate phase of Li_xRuO_2 to the fully lithiated mixed phase of Ru/Li_2O appeared only partially reversible. In line with this finding, Kim et al.[135] investigated the reaction mechanism of RuO_2 and found that, at the beginning of the discharge process, an intermediate phase-assisted transformation of RuO_2 to $LiRuO_2$ takes place and that the latter subsequently decomposes to nanosized Ru and Li_2O. In addition to its theoretical capacity, an excess reversible capacity was observed for lithiation voltages lower than 0.5 V, although the comprised Ru did not show any redox activity. Following the earlier work by Maier and co-workers, they assigned this to the Li storage at the grain boundaries between nanosized Ru^0 and Li_2O.

3.7. Other Transition Metal Oxides

Other TMOs such as Cr_2O_3 and MoO_x also offer high theoretical capacity values. Cr_2O_3, for instance, theoretically provides a capacity of 1058 mAh g^{-1} as lithium-ion anode, while simultaneously offering the lowest lithiation voltage (i.e., 0.2 V) among all TMOs described herein. In agreement with the proposed conversion mechanism, experiments revealed the complete reduction of the oxide to metallic chrome and Li_2O. The best charge capacity reported so far for the first cycle, however, has been well below 900 mAh g^{-1}, which led to rather low first cycle CEs. It has been reported that this limitation might be related to the partially irreversible reconversion of Cr_2O_3 to CrO only upon recharge to 3 V.[136] In addition, the cycling stability of powder-based electrodes remained rather poor in the existing literature without applying, e.g., a carbonaceous coating.[137,138] With regard to the volumetric capacity of such electrodes, though, the overall content of the carbon coating should be well controlled. The use of thin films has been reported as another effective strategy to enhance the cycling stability of Cr_2O_3[139] thanks to the extensive contact between the electrochemically active component and the current collector. Nevertheless, thin film electrodes are intrinsically restricted in terms of volumetric and gravimetric capacities when taking into account also the current collector (despite the absence of additional conductive additives, for instance), since for films thicker than 175 nm a dramatic performance fading has been observed.

Molybdenum oxides like MoO_3 have a theoretical specific capacity of 1117 mAh g^{-1}, but have been rarely investigated and accordingly there is little literature available to clearly state that these materials can achieve this value also upon continuous cycling. In fact, commonly a rapid capacity decay has been observed after several dis/charge cycles.[140,141] Another molybdenum oxide that has been investigated is MoO_2. First cycle discharge capacities well above its theoretical value (i.e., 838 mAh g^{-1}) have been reported[142] and stabilized capacities of about 700 mAh g^{-1} when the mesoporosity of the electrode was carefully controlled.[143,144] Ku et al.[145] developed an approach to further improve the electrochemical performance of MoO_2 by introducing a thermal activation at 120 °C during the first cycle. As a result, they observed capacities of around 800 mAh g^{-1} after 30 cycles. According to their X-ray photoelectron spectroscopy (XPS) and Raman spectroscopy analysis, MoO_2 was indeed reduced to Mo^0 upon lithiation and fully reoxidized to MoO_2 during the subsequent delithiation.

4. Summary and Outlook

The large family of conversion materials, i.e., compounds undergoing largely reversible conversion reactions with charge carriers like lithium or sodium, is an attractive class of materials to investigate whether the replacement of lithium by sodium might aid to overcome the previously identified challenges for the reversible charge storage. The reaction mechanisms in SIB electrodes can be, indeed, quite different due to the different phase stabilities. Throughout the sodiation and desodiation processes, sodium can form various stable oxides, like Na_2O, Na_2O_2, and NaO_2, while lithium-based materials are known to form basically Li_2O and Li_2O_2—mostly Li_2O. Hence, conversion reactions in SIBs may have more intermediate phases, offering a somehow richer electrochemical reactivity and potentially different reaction pathways. By studying and understanding the similarities and differences in crystallography, kinetics, and thermodynamics of the Li and Na-based conversion reactions, better battery performance may be achieved including the design of new material chemistries for both Li-ion and Na-ion applications. As such, a comprehensive comparative investigation may also shed further light into the greatest challenge for conversion-type active materials—the voltage hysteresis between the charge and discharge process. In fact, TMO-based conversion-type negative electrode active materials are, at present, mostly of academic interest until the remaining challenges will be overcome. The rather simple synthesis pathways for (transition) metal oxides allow for the development of advanced material architectures, targeting improved cycling stabilities and reaction kinetics. As such the corresponding research enables exploring the limits of what might also be possible for other kind of electrode materials and allow for the investigation of, e.g., electron-conducting self-healing binders to overcome the issues related to the low electronic conductivity of the oxides and the pronounced volume variation upon de/lithiation/sodiation, respectively. Also the optimization of

**ADVANCED
SCIENCE NEWS**

www.advancedsciencenews.com

**ADVANCED
ENERGY
MATERIALS**

www.advenergymat.de

the electrolyte composition for these highly reactive electrode materials—especially in the lithiated/sodiated state—might pave the way for finding advanced electrolyte compositions also for less catalytically active electrode materials. At least as (if not more) important, though, research efforts will have to focus on the identification of the underlying reaction mechanisms to understand them in detail, which is so far attracting less attention—not least because it is far more complicated. In this regard, this review article shall also serve as motivation for scientists to systematically study their reactivity as a function of the transition metal cation, its oxidation state, and the reversibly stored alkali metal cation. These aspects are becoming even more important when dealing with binary metal oxides—especially when different storage mechanisms are combined. It appears that the meaningful combination of electrochemical techniques and advanced physicochemical characterization techniques provides a viable way to do so, which, however, requires collaborative efforts of chemists, physicists, theoreticians, and engineers. While great progress has been achieved already since the seminal paper of Tarascon and co-workers, the detailed reaction mechanism and the definite origin of the voltage hysteresis are still unclear—for the electrochemical reaction with lithium as well as with sodium. As such, pure conversion-type anodes (and essentially also cathodes) are not foreseen to play a decisive role for commercial batteries in the near future. As a matter of fact, elements like cobalt, copper, chrome, or ruthenium will most likely not play a great role even if the underlying electrochemical reaction mechanism will be completely understood and methods to overcome these will have been found. However, materials like iron oxide or manganese oxide would be very attractive from an environmental and economic point of view. This certainly ambitious goal may justify the further investigation also of the less attractive ones, in case something valuable can be learnt. More importantly, though, it justifies the search for the major breakthrough(s) in understanding, as this would have a great impact on the technology.

Acknowledgements

Conflict of Interest

The authors declare no conflict of interest.

Keywords

[1] V. Etacheri, R. Marom, R. Elazari, G. Salitra, D. Aurbach, *Energy Environ. Sci.* **2011**, *4*, 3243.

[2] M. V. Reddy, G. V. S. Rao, B. V. R. Chowdari, *Chem. Rev.* **2013**, *113*, 5364.

[3] Y.-G. Guo, J.-S. Hu, L.-J. Wan, *Adv. Mater.* **2008**, *20*, 2878.

[4] D. Bresser, S. Passerini, B. Scrosati, *Energy Environ. Sci.* **2016**, *9*, 3348.

[5] P. K. Nayak, L. Yang, W. Brehm, P. Adelhelm, *Angew. Chem., Int. Ed.* **2018**, *57*, 102.

[6] B. Nykvist, M. Nilsson, *Nat. Clim. Change* **2015**, *5*, 329.

[7] Y. Yamada, Y. Iriyama, T. Abe, Z. Ogumi, *Langmuir* **2009**, *25*, 12766.

[8] N. Loeffler, D. Bresser, S. Passerini, M. Copley, *Platinum Met. Rev.* **2015**, *59*, 34.

[9] J. M. Tarascon, *Nat. Chem.* **2010**, *2*, 510.

[10] E. A. Olivetti, G. Ceder, G. G. Gaustad, X. Fu, *Joule* **2017**, *1*, 229.

[11] J. Y. Hwang, S. T. Myung, Y. K. Sun, *Chem. Soc. Rev.* **2017**, *46*, 3529.

[12] C. Vaalma, D. Buchholz, M. Weil, S. Passerini, *Nat. Rev. Mater.* **2018**, *3*, 18013.

[13] J. Mei, T. Liao, L. Kou, Z. Sun, *Adv. Mater.* **2017**, *29*, 1700176.

[14] S. Y. Huang, L. Kavan, I. Exnar, M. Grätzel, *J. Electrochem. Soc.* **1995**, *142*, L142.

[15] Z. Chen, I. Belharouak, Y. K. Sun, K. Amine, *Adv. Funct. Mater.* **2013**, *23*, 959.

[16] T. Ohzuku, A. Ueda, N. Yamamoto, *J. Electrochem. Soc.* **1995**, *142*, 1431.

[17] D. Bresser, E. Paillard, M. Copley, P. Bishop, M. Winter, S. Passerini, *J. Power Sources* **2012**, *219*, 217.

[18] P. Senguttuvan, G. Rousse, V. Seznec, J.-M. Tarascon, M. R. Palacín, *Chem. Mater.* **2011**, *23*, 4109.

[19] H. Pan, X. Lu, X. Yu, Y.-S. Hu, H. Li, X.-Q. Yang, L. Chen, *Adv. Energy Mater.* **2013**, *3*, 1186.

[20] Z. Yan, L. Liu, H. Shu, X. Yang, H. Wang, J. Tan, Q. Zhou, Z. Huang, X. Wang, *J. Power Sources* **2015**, *274*, 8.

[21] M. M. Doeff, J. Cabana, M. Shirpour, *J. Inorg. Organomet. Polym. Mater.* **2014**, *24*, 5.

[22] B. N. Loeffler, D. Bresser, S. Passerini, M. Copley, *Platinum Met. Rev.* **2015**, *59*, 34.

[23] T. Xu, W. Wei, M. L. Gordin, D. Wang, D. Choi, *JOM* **2010**, *62*, 24.

[24] F. Pan, J. Yang, Q. Huang, X. Wang, H. Huang, Q. Wang, *Adv. Energy Mater.* **2014**, *4*, 1400567.

[25] J. W. Choi, D. Aurbach, *Nat. Rev. Mater.* **2016**, *1*, 16013.

[26] M. N. Obrovac, V. L. Chevrier, *Chem. Rev.* **2014**, *114*, 11444.

[27] Y. Idota, *Science* **1997**, *276*, 1395.

[28] I. A. Courtney, *J. Electrochem. Soc.* **1997**, *144*, 2943.

[29] F. Belliard, J. Irvine, *J. Power Sources* **2001**, *97*, 219.

[30] J. Read, D. Foster, J. Wolfenstine, W. Behl, *J. Power Sources* **2001**, *96*, 277.

[31] C. J. Pelliccione, Y. Ding, E. V. Timofeeva, C. U. Segre, *J. Electrochem. Soc.* **2015**, *162*, A1935.

[32] P. Poizot, S. Laruelle, S. Grugeon, L. Dupont, J. M. Tarascon, *Nature* **2000**, *407*, 496.

[33] H. Zhang, I. Hasa, S. Passerini, *Adv. Energy Mater.* **2018**, *8*, 1702582.

[34] J. Cabana, L. Monconduit, D. Larcher, M. R. Palacín, *Adv. Mater.* **2010**, *22*, E170.

[35] N. Nitta, G. Yushin, *Part. Part. Syst. Charact.* **2014**, *31*, 317.

[36] F. Klein, B. Jache, A. Bhide, P. Adelhelm, *Phys. Chem. Chem. Phys.* **2013**, *15*, 15876.

[37] B. L. Ellis, P. Knauth, T. Djenizian, *Adv. Mater.* **2014**, *26*, 3368.

[38] J. Zhang, A. Yu, *Sci. Bull.* **2015**, *60*, 823.

[39] C. Yuan, H. B. Wu, Y. Xie, X. W. Lou, *Angew. Chem., Int. Ed.* **2014**, *53*, 1488.

[40] D. Mouad, Y. Naoaki, K. Kei, T. Kazuyasu, K. Shinichi, *Phys. Chem. Chem. Phys.* **2014**, *16*, 15007.

[41] W. Luo, F. Shen, C. Bommier, H. Zhu, X. Ji, L. Hu, *Acc. Chem. Res.* **2016**, *49*, 231.

**ADVANCED
SCIENCE NEWS**
www.advancedsciencenews.com

**ADVANCED
ENERGY
MATERIALS**
www.advenergymat.de

[42] D. Bresser, E. Paillard, P. Niehoff, S. Krueger, F. Mueller, M. Winter, S. Passerini, *ChemPhysChem* **2014**, *15*, 2177.

[43] C. Wu, S. X. Dou, Y. Yu, *Small* **2018**, *14*, 1703671.

[44] M. Valvo, F. Lindgren, U. Lafont, F. Björefors, K. Edström, *J. Power Sources* **2014**, *245*, 967.

[45] A. Eguia-Barrio, E. Castillo-Martínez, F. Klein, R. Pinedo, L. Lezama, J. Janek, P. Adelhelm, T. Rojo, *J. Power Sources* **2017**, *367*, 130.

[46] S. P. Ong, V. L. Chevrier, G. Hautier, A. Jain, C. Moore, S. Kim, X. Ma, G. Ceder, *Energy Environ. Sci.* **2011**, *4*, 3680.

[47] X. J. Zhu, Y. W. Zhu, S. Murali, M. D. Stollers, R. S. Ruoff, *ACS Nano* **2011**, *5*, 3333.

[48] J. Chen, L. N. Xu, W. Y. Li, X. L. Gou, *Adv. Mater.* **2005**, *17*, 582.

[49] M. V. Reddy, T. Yu, C. H. Sow, Z. X. Shen, C. T. Lim, G. V. S. Rao, B. V. R. Chowdari, *Adv. Funct. Mater.* **2007**, *17*, 2792.

[50] X. Xu, R. Cao, S. Jeong, J. Cho, *Nano Lett.* **2012**, *12*, 4988.

[51] A. Brandt, F. Winter, S. Klamor, F. Berkemeier, J. Rana, R. Pottgen, A. Balducci, *J. Mater. Chem. A* **2013**, *1*, 11229.

[52] G. Backert, B. Oschmann, M. N. Tahir, F. Mueller, I. Lieberwirth, B. Balke, W. Tremel, S. Passerini, R. Zentel, *J. Colloid Interface Sci.* **2016**, *478*, 155.

[53] L. Zhang, H. B. Wu, S. Madhavi, H. H. Hng, X. W. Lou, *J. Am. Chem. Soc.* **2012**, *134*, 17388.

[54] A. Brandt, A. Balducci, *J. Power Sources* **2013**, *230*, 44.

[55] B. Wang, J. S. Chen, H. B. Wu, Z. Y. Wang, X. W. Lou, *J. Am. Chem. Soc.* **2011**, *133*, 17146.

[56] V. Aravindan, N. Arun, N. Shubha, J. Sundaramurthy, S. Madhavi, *Electrochim. Acta* **2016**, *215*, 647.

[57] R. Verrelli, R. Brescia, A. Scarpellini, L. Manna, B. Scrosati, J. Hassoun, *RSC Adv.* **2014**, *4*, 618552.

[58] B. Q. Liu, Q. Zhang, Z. S. Jin, L. Y. Zhang, L. Li, Z. G. Gao, C. G. Wang, H. M. Xie, Z. M. Su, *Adv. Energy Mater.* **2018**, *8*, 1702347.

[59] J. S. Luo, J. L. Liu, Z. Y. Zeng, C. F. Ng, L. J. Ma, H. Zhang, J. Y. Lin, Z. X. Shen, H. J. Fan, *Nano Lett.* **2013**, *13*, 6136.

[60] W. Wei, S. B. Yang, H. X. Zhou, I. Lieberwirth, X. L. Feng, K. Mullen, *Adv. Mater.* **2013**, *25*, 2909.

[61] G. M. Zhou, D. W. Wang, F. Li, L. L. Zhang, N. Li, Z. S. Wu, L. Wen, G. Q. Lu, H. M. Cheng, *Chem. Mater.* **2010**, *22*, 5306.

[62] C. M. Ban, Z. C. Wu, D. T. Gillaspie, L. Chen, Y. F. Yan, J. L. Blackburn, A. C. Dillon, *Adv. Mater.* **2010**, *22*, E145.

[63] W. M. Zhang, X. L. Wu, J. S. Hu, Y. G. Guo, L. J. Wan, *Adv. Funct. Mater.* **2008**, *18*, 3941.

[64] C. N. He, S. Wu, N. Q. Zhao, C. S. Shi, E. Z. Liu, J. J. Li, *ACS Nano* **2013**, *7*, 4459.

[65] J. Ming, W. J. Kwak, S. J. Youn, H. Ming, J. Hassoun, Y. K. Sun, *Energy Technol.* **2014**, *2*, 778.

[66] H. Ming, J. Ming, S. M. Oh, S. Tian, Q. Zhou, H. Huang, Y. K. Sun, J. W. Zheng, *ACS Appl. Mater. Interfaces* **2014**, *6*, 15499.

[67] N. Zhang, X. P. Han, Y. C. Liu, X. F. Hu, Q. Zhao, J. Chen, *Adv. Energy Mater.* **2015**, *5*, 1401123.

[68] Y. Z. Jiang, M. J. Hu, D. Zhang, T. Z. Yuan, W. P. Sun, B. Xu, M. Yan, *Nano Energy* **2014**, *5*, 60.

[69] D.-Y. Park, S.-T. Myung, *ACS Appl. Mater. Interfaces* **2014**, *6*, 11749.

[70] Y. P. Zhou, W. P. Sun, X. H. Rui, Y. Zhou, W. J. Ng, Q. Y. Yan, E. Fong, *Nano Energy* **2016**, *21*, 71.

[71] H. Liu, M. Q. Jia, Q. Z. Zhu, B. Cao, R. J. Chen, Y. Wang, F. Wu, B. Xu, *ACS Appl. Mater. Interfaces* **2016**, *8*, 26878.

[72] G. H. Qin, J. Y. Duan, Y. C. Yang, F. S. Liu, *ACS Appl. Mater. Interfaces* **2018**, *10*, 6441.

[73] H. Qi, L. Cao, J. Li, J. Huang, Z. Xu, Y. Jie, C. Wang, *ChemistrySelect* **2019**, *4*, 2668.

[74] T. Guo, H. Liao, P. Ge, Y. Zhang, Y. Tian, W. Hong, Z. Shi, C. Shao, H. Hou, X. Ji, *Mater. Chem. Phys.* **2018**, *216*, 58.

[75] Y. Chen, X. Yuan, C. Yang, Y. Lian, A. A. Razzaq, R. Shah, J. Guo, X. Zhao, Y. Peng, Z. Deng, *J. Alloys Compd.* **2019**, *777*, 127.

[76] J. Ni, M. Sun, L. Li, *Adv. Mater.* **2019**, *31*, 1902603.

[77] W. Y. Li, L. N. Xu, J. Chen, *Adv. Funct. Mater.* **2005**, *15*, 851.

[78] Z. S. Wu, W. C. Ren, L. Wen, L. B. Gao, J. P. Zhao, Z. P. Chen, G. M. Zhou, F. Li, H. M. Cheng, *ACS Nano* **2010**, *4*, 3187.

[79] X. W. Lou, D. Deng, J. Y. Lee, J. Feng, L. A. Archer, *Adv. Mater.* **2008**, *20*, 258.

[80] Y. G. Li, B. Tan, Y. Y. Wu, *Nano Lett.* **2008**, *8*, 265.

[81] C. Yan, Y. Zhu, Y. Li, Z. Fang, L. Peng, X. Zhou, G. Chen, G. Yu, *Adv. Funct. Mater.* **2018**, *28*, 1705951.

[82] M. M. Rahman, A. M. Glushenkov, T. Ramireddy, Y. Chen, *Chem. Commun.* **2014**, *50*, 5057.

[83] Z. Jian, P. Liu, F. Li, M. Chen, H. Zhou, *J. Mater. Chem. A* **2014**, *2*, 13805.

[84] J. Jiang, C. Ma, T. Ma, J. Zhu, J. Liu, G. Yang, Y. Yang, *J. Alloys Compd.* **2019**, *794*, 385.

[85] H. Chen, L. Deng, S. Luo, X. Ren, Y. Li, L. Sun, P. Zhang, G. Chen, Y. Gao, *J. Electrochem. Soc.* **2018**, *165*, A3932.

[86] J. Li, D. Wang, J. Zhou, L. Hou, F. Gao, *ChemElectroChem* **2019**, *6*, 917.

[87] Y. Pang, S. Chen, C. Xiao, S. Ma, S. Ding, *J. Mater. Chem. A* **2019**, *7*, 4126.

[88] G. Longoni, M. Fiore, J. H. Kim, Y. H. Jung, D. K. Kim, C. M. Mari, R. Ruffo, *J. Power Sources* **2016**, *332*, 42.

[89] T. Chen, Z. Wu, W. Xiang, E. Wang, T. Chen, X. Guo, Y. Chen, B. Zhong, *Electrochim. Acta* **2017**, *246*, 931.

[90] W. Luo, X. Hu, Y. Sun, Y. Huang, *ACS Appl. Mater. Interfaces* **2013**, *5*, 1997.

[91] Y. Chu, L. Guo, B. Xi, Z. Feng, F. Wu, Y. Lin, J. Liu, D. Sun, J. Feng, Y. Qian, S. Xiong, *Adv. Mater.* **2018**, *30*, 1704244.

[92] G. Diao, M.-S. Balogun, S.-Y. Tong, X. Guo, X. Huang, Y. Mao, Y. Tong, *J. Mater. Chem. A* **2018**, *6*, 15274.

[93] A. L. M. Reddy, M. M. Shaijumon, S. R. Gowda, P. M. Ajayan, *Nano Lett.* **2009**, *9*, 1002.

[94] H. L. Wang, L. F. Cui, Y. A. Yang, H. S. Casalongue, J. T. Robinson, Y. Y. Liang, Y. Cui, H. J. Dai, *J. Am. Chem. Soc.* **2010**, *132*, 13978.

[95] L. Sheng, H. Jiang, S. Liu, M. Chen, T. Wei, Z. Fan, *J. Power Sources* **2018**, *397*, 325.

[96] Y.-C. Xiao, C.-Y. Xu, X.-Y. Sun, Y. Pei, P.-P. Wang, F.-X. Ma, L. Zhen, *Chem. Eng. J.* **2018**, *336*, 427.

[97] J. Gao, M. A. Lowe, H. D. Abruña, *Chem. Mater.* **2011**, *23*, 3223.

[98] Y. T. Weng, T. Y. Huang, C. H. Lim, P. S. Shao, S. Hy, C. Y. Kuo, J. H. Cheng, B. J. Hwang, J. F. Lee, N. L. Wu, *Nanoscale* **2015**, *7*, 20075.

[99] X. Zhang, G. Zhu, D. Yan, T. Lu, L. Pan, *J. Alloys Compd.* **2017**, *710*, 575.

[100] H. Li, A. Liu, S. Zhao, Z. Guo, N. Wang, T. Ma, *ChemElectroChem* **2018**, *5*, 3266.

[101] Y. He, P. Xu, B. Zhang, Y. Du, B. Song, X. Han, H. Peng, *ACS Appl. Mater. Interfaces* **2017**, *9*, 38401.

[102] A. Banerjee, U. Singh, V. Aravindan, M. Srinivasan, S. Ogale, *Nano Energy* **2013**, *2*, 1158.

[103] L. Hu, Y. Huang, F. Zhang, Q. Chen, *Nanoscale* **2013**, *5*, 4186.

[104] J. C. Park, J. Kim, H. Kwon, H. Song, *Adv. Mater.* **2009**, *21*, 803.

[105] G. Wang, Y. Sui, M. Zhang, M. Xu, Q. Zeng, C. Liu, X. Liu, F. Du, B. Zou, *J. Mater. Chem. A* **2017**, *5*, 18577.

[106] J. Wang, Q. Zhang, X. Li, D. Xu, Z. Wang, H. Guo, K. Zhang, *Nano Energy* **2014**, *6*, 19.

[107] S. F. Zheng, J. S. Hu, L. S. Zhong, W. G. Song, L. J. Wan, Y. G. Guo, *Chem. Mater.* **2008**, *20*, 3617.

[108] S. Ko, J. I. Lee, H. S. Yang, S. Park, U. Jeong, *Adv. Mater.* **2012**, *24*, 4451.

[109] S. Wu, G. Fu, W. Lv, J. Wei, W. Chen, H. Yi, M. Gu, X. Bai, L. Zhu, C. Tan, Y. Liang, G. Zhu, J. He, X. Wang, K. H. L. Zhang, J. Xiong, W. He, *Small* **2018**, *14*, 1870020.

1902485 (20 of 21)

**ADVANCED
SCIENCE NEWS**

www.advancedsciencenews.com

**ADVANCED
ENERGY
MATERIALS**

www.advenergymat.de

[110] R. Verrelli, J. Hassoun, A. Farkas, T. Jacob, B. Scrosati, *J. Mater. Chem. A* **2013**, *1*, 15329.

[111] R. Verrelli, B. Scrosati, Y. K. Sun, J. Hassoun, *ACS Appl. Mater. Interfaces* **2014**, *6*, 5206.

[112] R. Verrelli, N. Laszczynski, S. Passerini, J. Hassoun, *Energy Technol.* **2016**, *4*, 700.

[113] D. Di Lecce, R. Verrelli, D. Campanella, V. Marangon, J. Hassoun, *ChemSusChem* **2017**, *10*, 1607.

[114] W. Zhang, G. Ma, H. Gu, Z. Yang, H. Cheng, *J. Power Sources* **2015**, *273*, 561.

[115] S. Yuan, X. L. Huang, D. L. Ma, H. G. Wang, F. Z. Meng, X. B. Zhang, *Adv. Mater.* **2014**, *26*, 2273.

[116] Y. Li, M. Zhang, J. Qian, Y. Ma, Y. Li, W. Li, F. Wang, L. Li, F. Wu, R. Chen, *Energy Technol.* **2019**, *7*, 1900252.

[117] J. Ni, Y. Jiang, F. Wu, J. Maier, Y. Yu, L. Li, *Adv. Funct. Mater.* **2018**, *28*, 1707179.

[118] H. Liu, H. Zheng, L. Li, S. Jia, S. Meng, F. Cao, Y. Lv, D. Zhao, J. Wang, *Adv. Mater. Interfaces* **2018**, *5*, 1701255.

[119] L. Wang, K. Zhang, Z. Hu, W. Duan, F. Cheng, J. Chen, *Nano Res.* **2014**, *7*, 199.

[120] H. Liu, F. Cao, H. Zheng, H. Sheng, L. Li, S. Wu, C. Liu, J. Wang, *Chem. Commun.* **2015**, *51*, 10443.

[121] Y. Lu, N. Zhang, Q. Zhao, J. Liang, J. Chen, *Nanoscale* **2015**, *7*, 2770.

[122] U. Boesenberg, M. A. Marcus, A. K. Shukla, T. Yi, E. McDermott, P. F. Teh, M. Srinivasan, A. Moewes, J. Cabana, *Sci. Rep.* **2015**, *4*, 7133.

[123] B. Varghese, M. V. Reddy, Z. Yanwu, C. S. Lit, T. C. Hoong, G. V. S. Rao, B. V. R. Chowdari, A. T. S. Wee, C. T. Lim, C. H. Sow, *Chem. Mater.* **2008**, *20*, 3360.

[124] Y. Zou, Y. Wang, *Nanoscale* **2011**, *3*, 2615.

[125] G. M. Zhou, D. W. Wang, L. C. Yin, N. Li, F. Li, H. M. Cheng, *ACS Nano* **2012**, *6*, 3214.

[126] W. X. Guo, W. W. Sun, Y. Wang, *ACS Nano* **2015**, *9*, 11462.

[127] X. Wang, X. Li, X. Sun, F. Li, Q. Liu, Q. Wang, D. He, *J. Mater. Chem.* **2011**, *21*, 3571.

[128] K. He, F. Lin, Y. Zhu, X. Yu, J. Li, R. Lin, D. Nordlund, T. C. Weng, R. M. Richards, X. Q. Yang, M. M. Doeff, E. A. Stach, Y. Mo, H. L. Xin, D. Su, *Nano Lett.* **2015**, *15*, 5755.

[129] F. Zou, Y. M. Chen, K. Liu, Z. Yu, W. Liang, S. M. Bhaway, M. Gao, Y. Zhu, *ACS Nano* **2016**, *10*, 377.

[130] C. C. Yang, D. M. Zhang, L. Du, Q. Jiang, *J. Mater. Chem. A* **2018**, *6*, 12663.

[131] P. Balaya, H. Li, L. Kienle, J. Maier, *Adv. Funct. Mater.* **2003**, *13*, 621.

[132] H. Li, P. Balaya, J. Maier, *J. Electrochem. Soc.* **2004**, *151*, A1878.

[133] O. Delmer, P. Balaya, L. Kienle, J. Maier, *Adv. Mater.* **2008**, *20*, 501.

[134] K. E. Gregorczyk, Y. Liu, J. P. Sullivan, G. W. Rubloff, *ACS Nano* **2013**, *7*, 6354.

[135] Y. Kim, S. Muhammad, H. Kim, Y. H. Cho, H. Kim, J. M. Kim, W. S. Yoon, *ChemSusChem* **2015**, *8*, 2378.

[136] L. Dupont, S. Grugeon, S. Laruelle, J. M. Tarascon, *J. Power Sources* **2007**, *164*, 839.

[137] J. Hu, H. Li, X. J. Huang, *Electrochem. Solid-State Lett.* **2005**, *8*, A66.

[138] J. Hu, H. Li, X. J. Huang, L. Q. Chen, *Solid State Ionics* **2006**, *177*, 2791.

[139] S. Grugeon, S. Laruelle, L. Dupont, F. Chevallier, P. L. Taberna, P. Simon, L. Gireaud, S. Lascaud, E. Vidal, B. Yrieix, J. M. Tarascon, *Chem. Mater.* **2005**, *17*, 5041.

[140] S. H. Lee, Y. H. Kim, R. Deshpande, P. A. Parilla, E. Whitney, D. T. Gillaspie, K. M. Jones, A. H. Mahan, S. B. Zhang, A. C. Dillon, *Adv. Mater.* **2008**, *20*, 3627.

[141] Y. S. Jung, S. Lee, D. Ahn, A. C. Dillon, S. H. Lee, *J. Power Sources* **2009**, *188*, 286.

[142] Y. G. Liang, S. J. Yang, Z. H. Yi, J. T. Sun, Y. H. Zhou, *Mater. Chem. Phys.* **2005**, *93*, 395.

[143] X. L. Ji, S. Herle, Y. H. Rho, L. F. Nazar, *Chem. Mater.* **2007**, *19*, 374.

[144] Y. F. Shi, B. K. Guo, S. A. Corr, Q. H. Shi, Y. S. Hu, K. R. Heier, L. Q. Chen, R. Seshadri, G. D. Stucky, *Nano Lett.* **2009**, *9*, 4215.

[145] J. H. Ku, Y. S. Jung, K. T. Lee, C. H. Kim, S. M. Oh, *J. Electrochem. Soc.* **2009**, *156*, A688.